

$e^+e^-\gamma$ production at photon-photon colliders at complete
electroweak NLO accuracy

He-Yi Li,^{1,2} Ren-You Zhang,^{1,2,*} Wen-Gan Ma,^{1,2} Yi Jiang,^{1,2} and Xiao-Zhou Li^{1,2}

¹*State Key Laboratory of Particle Detection and Electronics,
University of Science and Technology of China,
Hefei 230026, Anhui, People's Republic of China*

²*Department of Modern Physics, University of Science and Technology of China,
Hefei 230026, Anhui, People's Republic of China*

(Dated: August 10, 2022)

arXiv:2208.04512v1 [hep-ph] 9 Aug 2022

Abstract

We present the NLO electroweak radiative corrections to the $e^+e^-\gamma$ production in $\gamma\gamma$ collision, which is an ideal channel for calibrating the beam luminosity of a Photon Linear Collider. We analyze the dependence of the total cross section on the beam colliding energy, and then investigate the kinematic distributions of final particles at various initial photon beam polarizations at EW NLO accuracy. The numerical results indicate that the EW relative corrections to the total cross section are non-negligible and become increasingly significant as the increase of the beam colliding energy, even can exceed -10% in the $J = 2$ $\gamma\gamma$ collision at $\sqrt{s} = 1$ TeV. Such EW corrections are very important and should be taken into consideration in precision theoretical and experimental studies at high-energy $\gamma\gamma$ colliders.

I. INTRODUCTION

There is a general consensus that the next large high-energy project after the Large Hadron Collider shall be a linear collider. As a potential extension to the positron-electron (e^+e^-) collision mode, the photon-photon ($\gamma\gamma$) collision [1, 2] at the International Linear Collider (ILC), i.e., the Photon Linear Collider (PLC), can help us to better understand the electroweak symmetry breaking and search for new physics beyond the standard model (BSM), such as supersymmetry, quantum gravity, extra dimensions, etc. Although the photon beam luminosity of PLC [3–5] can reach only approximately 80% of the electron beam luminosity at the ILC, the production rate of any charged particle pair in the $\gamma\gamma$ collision is typically about one order of magnitude higher than that in the e^+e^- collision. Therefore, the PLC provides a promising platform to test the standard model and search for BSM physics at the terascale. [6–8].

According to the “ILC Higgs White Paper” [2], the incoming photons at the high-energy PLC are produced via the backward Compton scattering (BCS) of the laser light off the linear electron beams [9, 10], which benefit from the monochromatic characteristic (concentrated at high energies in a narrow energy spread) and adjustable polarization mode. The $\gamma\gamma$ collision is known to have two polarization configurations: $J = 0$ and $J = 2$, where J denotes the total helicity of the two incoming photons. As is well known, $\gamma\gamma \rightarrow l^+l^-$ is the most promising

* Corresponding author: zhangry@ustc.edu.cn

channel for calibrating the photon beam luminosity of the the PLC [1, 4, 9, 11], and the precision predictions for the light fermion-antifermion pair production via $\gamma\gamma$ scattering up to the electroweak (EW) next-to-leading order (NLO) are given in [12, 13]. However, such a reaction is incapable of determining the luminosity of $J = 0$ polarized incoming photon beams, cause the production rate of this channel is suppressed by a factor of m_l^2/\hat{s} in the $J = 0$ polarization configuration [14]. On the other hand, as the $J = 0$ polarization mode is preferred by Higgs physics due to the unique channel $\gamma\gamma \rightarrow H^0 \rightarrow X$ (H^0 is any neutral scalar/pseudoscalar particle) in searching for BSM signals [15], the related high precision studies at $\gamma\gamma$ colliders are indispensable correspondingly. The $\gamma\gamma \rightarrow W^+W^-$ process is also proposed for measuring the photon luminosity of PLC [11], but it can only work for the circumstance with colliding energy exceeding the threshold of W -boson pair, and its cross section has to be measured precisely at first since such reaction could be accompanied by some BSM effects. Although the cross section for the $\gamma\gamma \rightarrow l^+l^-l^+l^-$ process is large and insensitive to the beam polarization, it is, unfortunately, rather small at large scattering angle where the lepton momenta can be measured precisely [3, 16].

Compared to the $\gamma\gamma \rightarrow l^+l^-$ process, the lepton pair production in association with an extra photon via $\gamma\gamma$ scattering is suppressed by an additional fine structure constant, but free from the helicity suppression due to the radiated spin-1 photon in the final state. Consequently, the $\gamma\gamma \rightarrow l^+l^-\gamma$ process can be adopted to measure the photon luminosity of the $J = 0$ $\gamma\gamma$ collision mode, and the precision theoretical predictions for $\gamma\gamma \rightarrow l^+l^-\gamma$ are necessary. Since the incoming photon beams at the PLC are only partially polarized, the ratio of the cross section for the $l^+l^-\gamma$ production via the $J = 0$ $\gamma\gamma$ scattering to that via $J = 2$ $\gamma\gamma$ scattering should be sufficiently high to calibrate the $J = 0$ $\gamma\gamma$ collision precisely. The dependences of the cross section for $\gamma\gamma \rightarrow l^+l^-\gamma$ on the helicity and colliding energy of the two incoming photons, as well as the kinematic cuts on the final state have already been analyzed at the lowest order [17, 18]. Careful and detailed studies show that the $\gamma\gamma \rightarrow l^+l^-\gamma$ process is a unique channel in measuring the photon luminosity together with the $\gamma\gamma \rightarrow l^+l^-$ process. In addition, the $e^+e^- \rightarrow l^+l^-$ and $e^+e^- \rightarrow l^+l^-\gamma$ processes also garner attention for determining the luminosity of the positron-electron collision mode at the ILC, and the related investigations at the EW NLO accuracy have been accomplished in [19, 20].

In this study, we calculate the complete NLO EW radiative corrections to the $e^+e^-\gamma$ production in $\gamma\gamma$ collision, and provide the integrated cross sections and some kinematic

distributions of final particles for both $J = 0$ and $J = 2$ polarization configurations. In Sec.II we describe in detail the analytical calculation strategy, and then present the numerical results and discussion for the integrated and differential cross sections in both inclusive and exclusive event selection schemes in Sec.III. Finally, a short summary is given in Sec.IV.

II. OUTLINE OF CALCULATIONS

A. LO calculation

We consider the process

$$\gamma_{\lambda_1}(q_1) + \gamma_{\lambda_2}(q_2) \rightarrow e_{h_1}^+(p_1) + e_{h_2}^-(p_2) + \gamma_{\lambda_3}(q_3), \quad (1)$$

where $\lambda_i = \pm$ and $q_i = (q_i^0 \equiv |\vec{q}_i|, \vec{q}_i)$ ($i = 1, 2, 3$) are the helicities and four-momenta of the incoming and outgoing photons, while $h_j = \pm$ and $p_j = (p_j^0 \equiv \sqrt{|\vec{p}_j|^2 + m_e^2}, \vec{p}_j)$ ($j = 1, 2$) are the helicities and four-momenta of the two final-state fermions (positron and electron). Then, the total helicity of the two incoming photons is given by $J = |\lambda_1 - \lambda_2|$. We denote the differential cross section in the center-of-mass (c.m.) frame of the initial-state $\gamma\gamma$ system as $d\hat{\sigma}^{\lambda_1\lambda_2h_1h_2\lambda_3}(\vec{q}_1, \vec{q}_2; \vec{p}_1, \vec{p}_2, \vec{q}_3)$. If the two incoming photon beams are partially polarized, the differential cross section for the unpolarized $e^+e^-\gamma$ production (i.e., the polarizations of the final-state e^+ , e^- and γ are not measured) in $\gamma\gamma$ collision is given by [21]

$$d\hat{\sigma}(\mathcal{P}_1, \mathcal{P}_2; \vec{q}_1, \vec{q}_2; \vec{p}_1, \vec{p}_2, \vec{q}_3) = \frac{1}{4} \sum_{\lambda_{1,2}=\pm} (1 + \lambda_1\mathcal{P}_1)(1 + \lambda_2\mathcal{P}_2) d\hat{\sigma}^{\lambda_1\lambda_2}(\vec{q}_1, \vec{q}_2; \vec{p}_1, \vec{p}_2, \vec{q}_3), \quad (2)$$

where \mathcal{P}_1 and \mathcal{P}_2 are the degrees of polarization of the two incoming photon beams¹, and

$$d\hat{\sigma}^{\lambda_1\lambda_2}(\vec{q}_1, \vec{q}_2; \vec{p}_1, \vec{p}_2, \vec{q}_3) = \sum_{\lambda_3, h_{1,2}=\pm} d\hat{\sigma}^{\lambda_1\lambda_2h_1h_2\lambda_3}(\vec{q}_1, \vec{q}_2; \vec{p}_1, \vec{p}_2, \vec{q}_3). \quad (3)$$

The tree-level Feynman diagrams for $\gamma\gamma \rightarrow e^+e^-\gamma$ are depicted in Fig.1. By using \mathcal{C} , \mathcal{P} , \mathcal{CP} and *Bose* symmetries [18], we obtain

$$\begin{aligned} \mathcal{C} : \quad & d\hat{\sigma}_{\text{LO}}^{\lambda_1\lambda_2h_1h_2\lambda_3}(\vec{q}_1, \vec{q}_2; \vec{p}_1, \vec{p}_2, \vec{q}_3) = d\hat{\sigma}_{\text{LO}}^{\lambda_1\lambda_2h_2h_1\lambda_3}(\vec{q}_1, \vec{q}_2; \vec{p}_2, \vec{p}_1, \vec{q}_3) \\ \mathcal{P} : \quad & d\hat{\sigma}_{\text{LO}}^{\lambda_1\lambda_2h_1h_2\lambda_3}(\vec{q}_1, \vec{q}_2; \vec{p}_1, \vec{p}_2, \vec{q}_3) = d\hat{\sigma}_{\text{LO}}^{-\lambda_1-\lambda_2-h_1-h_2-\lambda_3}(-\vec{q}_1, -\vec{q}_2; -\vec{p}_1, -\vec{p}_2, -\vec{q}_3) \\ \mathcal{CP} : \quad & d\hat{\sigma}_{\text{LO}}^{\lambda_1\lambda_2h_1h_2\lambda_3}(\vec{q}_1, \vec{q}_2; \vec{p}_1, \vec{p}_2, \vec{q}_3) = d\hat{\sigma}_{\text{LO}}^{-\lambda_1-\lambda_2-h_2-h_1-\lambda_3}(-\vec{q}_1, -\vec{q}_2; -\vec{p}_2, -\vec{p}_1, -\vec{q}_3) \\ \textit{Bose} : \quad & d\hat{\sigma}_{\text{LO}}^{\lambda_1\lambda_2h_1h_2\lambda_3}(\vec{q}_1, \vec{q}_2; \vec{p}_1, \vec{p}_2, \vec{q}_3) = d\hat{\sigma}_{\text{LO}}^{\lambda_2\lambda_1h_1h_2\lambda_3}(\vec{q}_2, \vec{q}_1; \vec{p}_1, \vec{p}_2, \vec{q}_3) \end{aligned} \quad (4)$$

¹ The degree of polarization of a photon beam is defined as $\mathcal{P} = \frac{N_+ - N_-}{N_+ + N_-}$, where N_+ and N_- are the numbers of right- and left-handed photons, respectively.

It should be noted that \mathcal{C} and \mathcal{P} are simply the Born-level symmetries for the $\gamma\gamma \rightarrow e^+e^-\gamma$ process, because $\gamma\gamma \rightarrow e^+e^-\gamma$ is a pure QED scattering process at the lowest order, and the weak interaction is only involved in the high-order radiative corrections. From Eq.(4) we obtain

$$\begin{aligned} \mathcal{CP} + Bose : \quad d\hat{\sigma}^{--}(\vec{q}_1, \vec{q}_2; \vec{p}_1, \vec{p}_2, \vec{q}_3) &= d\hat{\sigma}^{++}(-\vec{q}_2, -\vec{q}_1; -\vec{p}_2, -\vec{p}_1, -\vec{q}_3) \\ d\hat{\sigma}^{+-}(\vec{q}_1, \vec{q}_2; \vec{p}_1, \vec{p}_2, \vec{q}_3) &= d\hat{\sigma}^{+-}(-\vec{q}_2, -\vec{q}_1; -\vec{p}_2, -\vec{p}_1, -\vec{q}_3) \end{aligned} \quad (5)$$

It clearly demonstrates that the differential distributions as well as the integrated cross section for $\gamma_-\gamma_-$ collisions can be obtained straightforwardly from the corresponding ones for $\gamma_+\gamma_+$ collisions. Therefore in the following discussion, we only consider the $\gamma_+\gamma_+ \rightarrow e^+e^-\gamma$ and $\gamma_+\gamma_- \rightarrow e^+e^-\gamma$ channels for $J = 0$ and $J = 2$ polarization configurations of the $\gamma\gamma$ system, respectively. Moreover, we can conclude that the final-state electron and positron in the $J = 2$ collision mode should have identical kinematic behaviors from Eq.(5), while there is no such coincidental feature in the $J = 0$ collision mode.

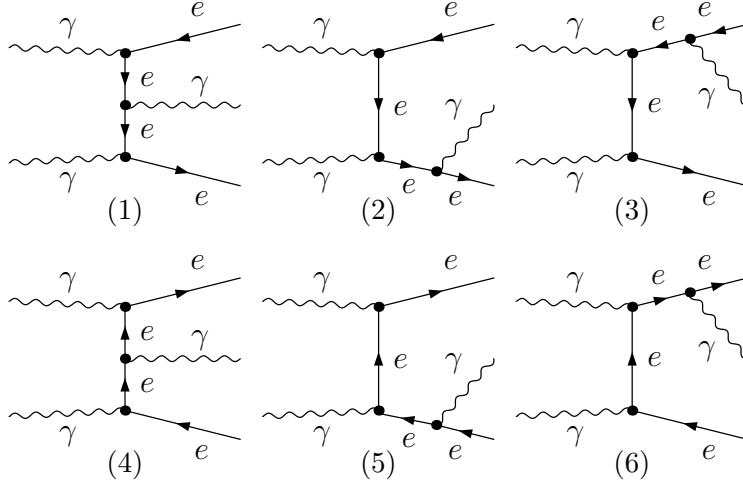


FIG. 1. Leading order Feynman diagrams for $\gamma\gamma \rightarrow e^+e^-\gamma$.

The leading order (LO) differential cross section for $\gamma_{\lambda_1}(q_1) + \gamma_{\lambda_2}(q_2) \rightarrow e_{h_1}^+(p_1) + e_{h_2}^-(p_2) + \gamma_{\lambda_3}(q_3)$ can be expressed as

$$d\hat{\sigma}_{\text{LO}}^{\lambda_1\lambda_2h_1h_2\lambda_3}(\vec{q}_1, \vec{q}_2; \vec{p}_1, \vec{p}_2, \vec{q}_3) = \frac{1}{2\hat{s}} |\mathcal{M}_{\text{LO}}^{\lambda_1\lambda_2h_1h_2\lambda_3}(\vec{q}_1, \vec{q}_2; \vec{p}_1, \vec{p}_2, \vec{q}_3)|^2 d\Phi_3(\vec{p}_1, \vec{p}_2, \vec{q}_3), \quad (6)$$

where $\hat{s} = (q_1 + q_2)^2$, $\mathcal{M}_{\text{LO}}^{\lambda_1\lambda_2h_1h_2\lambda_3}(\vec{q}_1, \vec{q}_2; \vec{p}_1, \vec{p}_2, \vec{q}_3)$ is the LO helicity amplitude that can be acquired by applying the Weyl-van-der-Waerden spinor technique [14, 22, 23], and

$d\Phi_3(\vec{p}_1, \vec{p}_2, \vec{q}_3)$ represents the $e^+e^-\gamma$ final-state phase-space element, which is given by

$$d\Phi_3(\vec{p}_1, \vec{p}_2, \vec{q}_3) = (2\pi)^4 \delta^{(4)}(p_1 + p_2 + q_3 - q_1 - q_2) \frac{d^3\vec{p}_1}{(2\pi)^3 2p_1^0} \frac{d^3\vec{p}_2}{(2\pi)^3 2p_2^0} \frac{d^3\vec{q}_3}{(2\pi)^3 2q_3^0}. \quad (7)$$

In the limit of $m_e \rightarrow 0$, $\mathcal{M}_{\text{LO}}^{\lambda_1\lambda_2h_1h_2\lambda_3} = 0$ if $h_1 = h_2$ or $\lambda_1 = \lambda_2 = -\lambda_3$. All the non-vanishing LO helicity amplitudes can be obtained from $\mathcal{M}_{\text{LO}}^{+-+}$ by using \mathcal{C} , \mathcal{P} and *Bose* symmetries in Eq.(4), and the crossing symmetry between the initial and final photons [18]. By adopting the helicity amplitude method [22], we obtain

$$|\mathcal{M}_{\text{LO}}^{+-+}(\vec{q}_1, \vec{q}_2; \vec{p}_1, \vec{p}_2, \vec{q}_3)|^2 = 4e^6 \frac{(p_1 \cdot p_2)(p_2 \cdot q_2)^2}{(p_1 \cdot q_1)(p_1 \cdot q_3)(p_2 \cdot q_1)(p_2 \cdot q_3)}. \quad (8)$$

B. NLO EW corrections

We employ the modified FEYNARTS-3.7+FORMCALC-7.3+LOOPTOOLS-2.8 packages [24–26] to generate Feynman diagrams, simplify Feynman amplitudes, and perform loop and phase-space integrations. The one-loop EW virtual correction to $\gamma\gamma \rightarrow e^+e^-\gamma$ includes 960 Feynman diagrams, which can be categorized into self-energy (36), triangle (438), box (414), pentagon (42) and counterterm (30) diagrams. Some representative box and pentagon Feynman diagrams for $\gamma\gamma \rightarrow e^+e^-\gamma$ are depicted in Fig.2. We can see that the loop diagram in Fig.2 (2) may induce Z resonance in the vicinity of $M_{e^+e^-} = m_Z$, where $M_{e^+e^-}$ is the invariant mass of the final-state e^+e^- system, due to the possible on-shell Z propagator. To avoid the numerical divergence in loop calculation, we replace the Z propagator $1/(p^2 - m_Z^2)$ by $1/(p^2 - m_Z^2 - im_Z\Gamma_Z)$, where the contribution from the imaginary part is beyond the EW NLO and thus can be ignored. We adopt the dimensional regularization (DR) scheme [27] to regularize the ultraviolet (UV) divergences. In the DR scheme, the dimensions of spinor and space-time manifolds are all extended to $D = 4 - 2\epsilon$. The 5-point loop integrals are decomposed into 4-point loop integrals by adopting the Denner-Dittmaier method [28], and all the N -point ($N \leq 4$) tensor integrals are reduced into scalar integrals recursively by adopting the Passarino-Veltman reduction algorithm [29]. In the calculation of 4-point scalar integrals, numerical instability would occur at some phase-space regions with small Gram determinants. Generally, this problem can be solved by adopting the quadruple precision arithmetic proposed in [30].

The renormalized electric charge is defined by $e^{(B)} = (1 + \delta Z_e)e$, where $e^{(B)}$ is the bare electric charge and δZ_e is the corresponding renormalization constant. We adopt the $\alpha(0)$

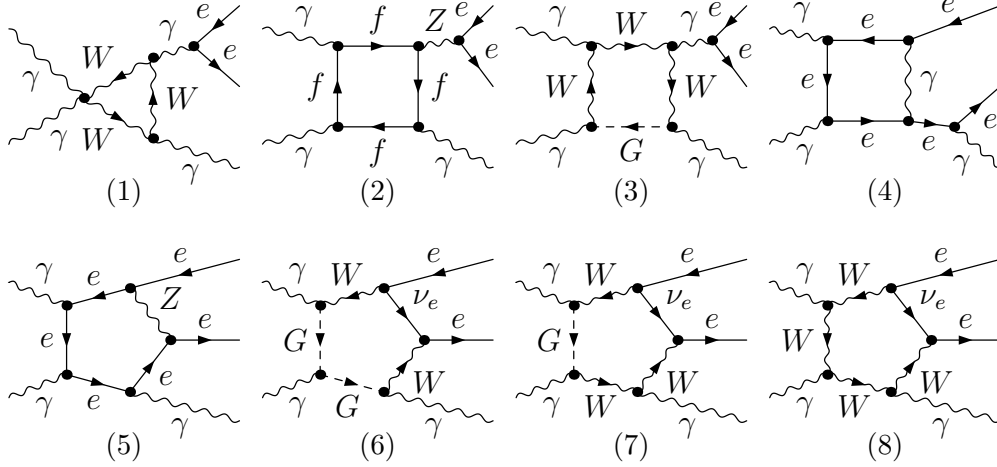


FIG. 2. Representative box and pentagon Feynman diagrams for $\gamma\gamma \rightarrow e^+e^-\gamma$.

scheme to renormalize the electric charge, in which the fine structure constant is set to its Thomson limit $\alpha(0)$ and the electric charge renormalization constant $\delta Z_e^{\alpha(0)}$ is given by [31]

$$\delta Z_e^{\alpha(0)} = -\frac{1}{2}\delta Z_{AA} - \frac{1}{2}\tan\theta_W\delta Z_{ZA} = \frac{1}{2}\frac{\partial \sum_T^{AA}(p^2)}{\partial p^2}\Bigg|_{p^2=0} - \tan\theta_W\frac{\sum_T^{AZ}(0)}{m_Z^2}, \quad (9)$$

where θ_W is the weak mixing angle and \sum_T^{ab} represents the transverse part of the unrenormalized self-energy of the $a \rightarrow b$ transition. For the field and mass renormalization, we employ the on-mass-shell scheme. The definitions and expressions of the relevant renormalization constants in the on-mass-shell scheme can be found in [31]. After performing the renormalization procedure, all the UV singularities are canceled and thus the virtual correction is UV finite.

The virtual photon in loops can induce soft and quasi-collinear infrared (IR) divergences. We introduce an infinitesimal fictitious photon mass to regularize IR divergences. According to the Kinoshita-Lee-Nauenberg (KLN) theorem [32, 33], we should consider the contribution from the real photon emission process $\gamma\gamma \rightarrow e^+e^-\gamma\gamma$ to get IR-safe observables at the EW NLO. The IR divergences of the virtual correction can be canceled exactly by those of the real photon emission correction. We extract the IR singularities from the real emission correction by employing the dipole subtraction (DS) method [34–37] and combine them with the virtual correction. In the DS method, a parameter $\alpha \in (0, 1]$ is introduced to control the subtraction region [38, 39], but the total cross section is independent of α . We also employ the two cutoff phase space slicing (TCPSS) method [40] to deal with the real

photon emission process for comparison, and find that the integrated cross sections obtained by using the DS and TCPSS methods are in good agreement with each other within the calculation errors.

C. $ee \rightarrow \gamma\gamma \rightarrow e^+e^-\gamma$ at the PLC

Among all the methods of $e \rightarrow \gamma$ conversion, the best one is BCS of laser light on high energy electrons. The photons after BCS have energy close to that of the initial electrons and follow their directions with some small angular spread. Given that the photon beams at the PLC are generated via BCS mechanism, $\gamma\gamma \rightarrow e^+e^-\gamma$ can be regarded as the subprocess of $ee \rightarrow \gamma\gamma \rightarrow e^+e^-\gamma$. The production cross section for the parent process $ee \rightarrow \gamma\gamma \rightarrow e^+e^-\gamma$ can be obtained by folding the cross section for $\gamma\gamma \rightarrow e^+e^-\gamma$ with the photon luminosity, i.e.,

$$\sigma(ee \rightarrow \gamma\gamma \rightarrow e^+e^-\gamma; s) = \int_{2m_e/\sqrt{s}}^{x_{\max}} dz \frac{d\mathcal{L}_{\gamma\gamma}}{dz}(z) \hat{\sigma}(\gamma\gamma \rightarrow e^+e^-\gamma; \hat{s} = z^2 s), \quad (10)$$

where \sqrt{s} and $\sqrt{\hat{s}}$ are the c.m. colliding energies of ee and $\gamma\gamma$ systems, respectively. The photon luminosity is given by

$$\frac{d\mathcal{L}_{\gamma\gamma}}{dz}(z) = 2z \int_{z^2/x_{\max}}^{x_{\max}} \frac{dx}{x} \phi_{\gamma/e}(x) \phi_{\gamma/e}(z^2/x), \quad (11)$$

where $\phi_{\gamma/e}(x)$ denotes the photon structure function, and x is the fraction of the energy of the incident electron carried by the back-scattered photon. As is well known, the degree of polarization of the back-scattered photon \mathcal{P}_γ is also a function of the energy fraction x . Both $\phi_{\gamma/e}$ and \mathcal{P}_γ depend on the degrees of polarization of the incident electron and laser light. In the numerical treatment, the structure function $\phi_{\gamma/e}(x)$, polarization degree function $\mathcal{P}_\gamma(x)$, and maximum energy fraction x_{\max} of the back-scattered photon are all obtained from COMPАЗ [5], whose parametrization is based on a realistic TESLA prototype [41].

Finally, the NLO EW corrected cross section for $ee \rightarrow \gamma\gamma \rightarrow e^+e^-\gamma$ is given by

$$\sigma_{\text{NLO}} = \sigma_{\text{LO}} + (1 + \delta_{\text{EW}}), \quad \delta_{\text{EW}} = \frac{\Delta\sigma_{\text{vir}} + \Delta\sigma_{\text{real}}}{\sigma_{\text{LO}}}, \quad (12)$$

where the NLO EW relative correction δ_{EW} can be decomposed into QED and genuine weak relative corrections, i.e., $\delta_{\text{EW}} = \delta_{\text{QED}} + \delta_{\text{W}}$. The same definitions also hold for $\gamma\gamma \rightarrow e^+e^-\gamma$ by substituting σ with $\hat{\sigma}$. In the following discussion on the $\gamma\gamma \rightarrow e^+e^-\gamma$ channel, the superscript “ $\hat{}$ ” in $\hat{\sigma}$ will be omitted only for convenience.

III. NUMERICAL RESULTS AND DISCUSSION

In this section, we provide the total cross sections and kinematic distributions of final particles for $\gamma\gamma \rightarrow e^+e^-\gamma$ up to the EW NLO for both $J = 0$ and $J = 2$ photon beam polarization configurations. Some kinematic cuts are imposed on the final state to exclude inevitable infrared divergences and fulfil the experimental requirement in the luminosity measurement.

A. Event selection criteria

At the EW NLO, both $\gamma\gamma \rightarrow e^+e^-\gamma$ and $\gamma\gamma \rightarrow e^+e^-\gamma\gamma$ channels are involved in the production of $e^+e^-\gamma$ at the PLC. When generating $e^+e^-\gamma$ event samples and calculating cross sections at the LO, the following set of kinematic and geometric acceptance requirements are applied on the final-state electron, positron and photon as event selection cuts:

$$\begin{aligned}
 \text{energies:} & \quad E_{e^\pm}, E_\gamma \geq 10 \text{ GeV} \\
 \text{scattering angles:} & \quad \theta_{e^\pm}, \theta_\gamma \in [10^\circ, 170^\circ] \\
 \text{opening angles:} & \quad \theta_{e^\pm\gamma}, \theta_{e^+e^-} \geq 10^\circ
 \end{aligned}
 \tag{13}$$

where θ_i ($i = e^\pm, \gamma$) denotes the scattering angle of the final-state particle i with respect to the incoming “+”-polarized photon beam direction, and θ_{ij} ($ij = e^\pm\gamma, e^+e^-$) represents the opening angle between i and j in the c.m. frame of the initial-state $\gamma\gamma$ system. This set of kinematic cuts can also guarantee the IR safety at the LO, and all the final-state particles are well separated.

For the $\gamma\gamma \rightarrow e^+e^-\gamma\gamma$ channel, the two tracks of the $\gamma\gamma$ - or γe^\pm -pair will be recombined as a quasi-particle if they are sufficiently collinear ($\theta_{\gamma\gamma}$ or $\theta_{e^\pm\gamma} \leq 10^\circ$), and the final state is regarded as an $e^+e^-\gamma$ event; otherwise, it is categorized as an $e^+e^-\gamma\gamma$ event. In this study, we adopt both inclusive and exclusive event selection schemes in the numerical calculations. In the inclusive event selection scheme (denoted by scheme-I), only the baseline event selection cuts in Eq.(13) are applied on the $e^+e^-\gamma$ and $e^+e^-\gamma\gamma$ events. It should be noted that only one of the two final-state photons needs to satisfy the kinematic constraints in Eq.(13) for an $e^+e^-\gamma\gamma$ event. Hence, the events with two energetic and well separated photons are accepted in the inclusive event selection scheme. In contrast, an $e^+e^-\gamma\gamma$ event will be rejected in the

exclusive event selection scheme (denoted by scheme-II) if both final-state photons can pass the kinematic cuts in Eq.(13).

B. Input parameters

The SM input parameters used in this paper are taken as [42]

$$\begin{aligned}
m_e &= 0.5109989461 \text{ MeV} & m_\mu &= 105.6583745 \text{ MeV} & m_\tau &= 1776.86 \text{ MeV} \\
m_u &= 62 \text{ MeV} & m_c &= 1.5 \text{ GeV} & m_t &= 172.76 \text{ GeV} \\
m_d &= 83 \text{ GeV} & m_s &= 215 \text{ MeV} & m_b &= 4.7 \text{ GeV} \\
m_W &= 80.379 \text{ GeV} & m_Z &= 91.1876 \text{ GeV} & \Gamma_Z &= 2.4952 \text{ GeV} \\
\alpha(0) &= 1/137.035999084
\end{aligned} \tag{14}$$

where the masses of light quarks can reproduce the hadronic contribution to the photon vacuum polarization [43], and $\alpha(0)$ is the fine structure constant in the Thomson limit.

Normally, there exists mass-singular terms $\log(m_f^2/\mu^2)$ in both the electric charge renormalization constant and the photon wave-function renormalization constant. If the number of external photons equals that of the EW couplings in the tree-level amplitude, the full NLO EW correction is free of these unpleasant large logarithms because of the exact cancellation between the logarithms in the vertex counterterm and in the photon wave-function counterterm. Therefore, it is reasonable to adopt the $\alpha(0)$ scheme for all the EW couplings involved in the $\gamma\gamma \rightarrow e^+e^-\gamma$ process.

C. Integrated cross sections

In order to verify the correctness of our numerical calculations for the integrated cross section, we perform the following checks:

- We calculate the LO cross section for $\gamma\gamma \rightarrow e^+e^-\gamma$ in $J = 0$ collision at $\sqrt{\hat{s}} = 500 \text{ GeV}$ by employing our developed FEYNARTS-3.7+FORMCALC-7.3+LOOPTOOLS-2.8 and MADGRAPH5-2.3.3 [44] packages, respectively, and obtain

$$\sigma_{\text{LO}} [\text{pb}] = \begin{cases} 0.042817(5) & (\text{FeynArts+FormCalc+LoopTools}) \\ 0.04279(1) & (\text{MadGraph}) \end{cases} \tag{15}$$

These two results are in good agreement with each other.

- We verify numerically the independence of the full NLO EW corrected cross section on the fictitious photon mass m_γ in the range of $10^{-15} \leq m_\gamma/\text{GeV} \leq 1$.
- We calculate the NLO EW corrected cross section for $\gamma\gamma \rightarrow e^+e^-\gamma$ in $J = 0$ collision at $\sqrt{\hat{s}} = 250, 500, 1000$ GeV in scheme-I by adopting the DS (with $\alpha = 0.1$) and TCPSS (with $\delta_s = \delta_c = 0.001$) methods separately, and find that the numerical results (shown in Table I) are coincident with each other within the calculation errors.

$\sqrt{\hat{s}}$ [GeV]		250	500	1000
$\sigma_{\text{NLO}}^{(\text{I})}$ [pb]	DS	0.15534(4)	0.04261(2)	0.01090(1)
	TCPSS	0.15525(9)	0.04260(3)	0.01092(2)

TABLE I. NLO EW corrected cross sections for $\gamma\gamma \rightarrow e^+e^-\gamma$ in $J = 0$ collision at $\sqrt{\hat{s}} = 250, 500, 1000$ GeV in the inclusive event selection scheme obtained by using the DS and TCPSS methods separately.

In further numerical calculations, we adopt only the DS method with $\alpha = 0.1$, and fix the fictitious photon mass as $m_\gamma = 10^{-2}$ GeV. For brevity's sake, the NLO EW corrected cross sections and the corresponding EW and pure QED relative corrections in the inclusive and exclusive event selection schemes are denoted by $\sigma_{\text{NLO}}^{(\text{I, II})}$, $\delta_{\text{EW}}^{(\text{I, II})}$ and $\delta_{\text{QED}}^{(\text{I, II})}$, respectively. Since the colliding energy dependence of the NLO EW corrected integrated cross section and differential distributions in scheme-I are almost the same as the LO predictions, we only depict the integrated and differential cross sections in scheme-II in the following discussion.

In Figs.3 (a) and (b), we present the integrated cross sections σ_{LO} , $\sigma_{\text{NLO}}^{(\text{II})}$ (in upper panels) and the corresponding EW relative corrections $\delta_{\text{EW}}^{(\text{I, II})}$ (in lower panels) as functions of the $\gamma\gamma$ c.m. colliding energy for the $e^+e^-\gamma$ production in $J = 0$ and $J = 2$ $\gamma\gamma$ collisions, respectively. As shown in this figure, the LO and NLO EW corrected cross sections for $\gamma\gamma \rightarrow e^+e^-\gamma$ in both $J = 0$ and $J = 2$ $\gamma\gamma$ collision modes decrease quickly as $\sqrt{\hat{s}}$ increases from 120 GeV to 1 TeV. The EW relative correction is sensitive to the $\gamma\gamma$ colliding energy. In the inclusive event selection scheme, it increases in the low colliding energy region, reaches its maximum at $\sqrt{\hat{s}} \sim 300$ and 160 GeV for the $J = 0$ and $J = 2$ collision modes, respectively, and then decreases gradually as the increase of $\sqrt{\hat{s}}$. In the exclusive event selection scheme, the EW relative correction is negative in the plotted $\sqrt{\hat{s}}$ region. It decreases monotonically from

−2.30% to −9.20% and from −2.36% to −10.65% for $J = 0$ and $J = 2$, respectively, as $\sqrt{\hat{s}}$ varies from 120 GeV to 1 TeV.

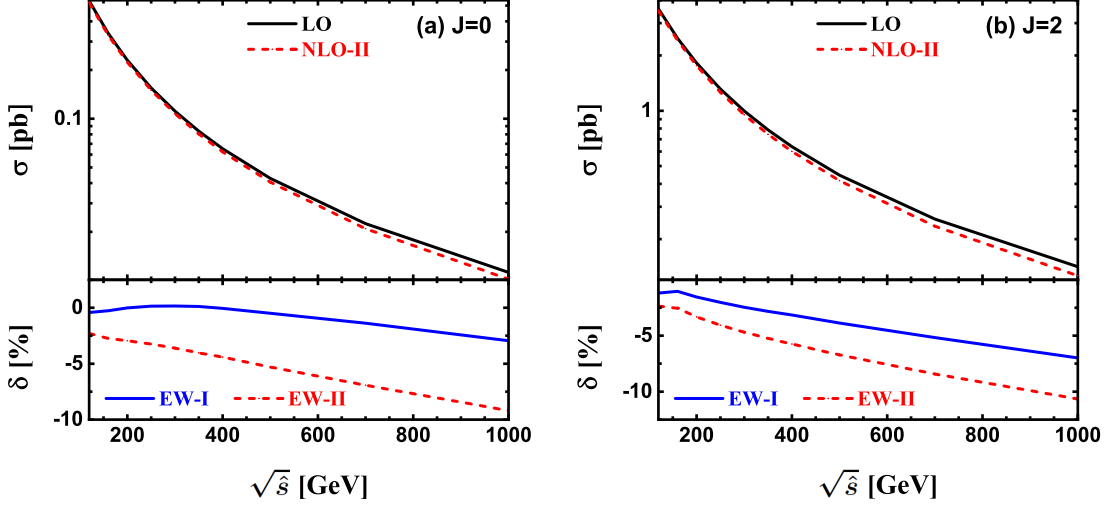


FIG. 3. LO, NLO EW corrected integrated cross sections in scheme-II and the EW relative corrections in both scheme-I and -II as functions of $\sqrt{\hat{s}}$ for the $e^+e^-\gamma$ production in (a) $J = 0$ and (b) $J = 2$ $\gamma\gamma$ collisions.

To analyze the constituents of the NLO EW correction more clearly, we depict the dependence of the pure QED and genuine weak relative corrections in both inclusive and exclusive event selection schemes on the $\gamma\gamma$ colliding energy for the $e^+e^-\gamma$ production in $J = 0$ and $J = 2$ $\gamma\gamma$ collisions in Figs.4 (a) and (b) separately². In the exclusive event selection scheme, both QED and genuine weak relative corrections strongly depend on the $\gamma\gamma$ colliding energy, and the full NLO EW correction is dominated by the QED correction. As $\sqrt{\hat{s}}$ increases from 120 GeV to 1 TeV, the pure QED relative correction decreases consistently from −2.23% to −5.87% for the $J = 0$ collision mode, and from −2.40% to −6.89% for the $J = 2$ collision mode. Compared to the QED relative correction, the weak relative correction is not a monotonically decreasing function of $\sqrt{\hat{s}}$. It can be seen from Fig.4 (b) that there is a small peak at $\sqrt{\hat{s}} \simeq 2m_W \simeq 160$ GeV in the colliding energy distribution of the weak relative correction to the $e^+e^-\gamma$ production via $J = 2$ $\gamma\gamma$ collision, which corresponds to the W -pair resonance induced by the triangle loop in Fig.2 (1). For both the $J = 0$ and $J = 2$ collision

² The weak relative correction in the exclusive scheme is the same as that in the inclusive scheme.

modes, the weak relative correction is small ($|\delta_W| < 0.5\%$) when $\sqrt{\hat{s}} < 300$ GeV, while it becomes relatively remarkable in the high energy region due to the Sudakov logarithms induced by the virtual exchange of soft or collinear massive weak gauge bosons [45, 46]. At $\sqrt{\hat{s}} = 1$ TeV, $(\delta_W, \delta_{EW}^{(II)}) = (-3.33\%, -9.20\%)$ and $(-3.76\%, -10.65\%)$ for $J = 0$ and $J = 2$, respectively. It clearly shows that the full EW relative correction to $e^+e^-\gamma$ production in the exclusive event selection scheme can reach and even exceed -10% at a TeV PLC. In the inclusive event selection scheme, the QED relative correction contributed by $e^+e^-\gamma\gamma$ events, i.e., $\delta_{QED}^{(I)} - \delta_{QED}^{(II)}$, is sizable, especially in the high energy region. It increases gradually from 1.88% to 6.26% and from 1.09% to 3.49% for $J = 0$ and $J = 2$, respectively, as $\sqrt{\hat{s}}$ increases from 120 GeV to 1 TeV.

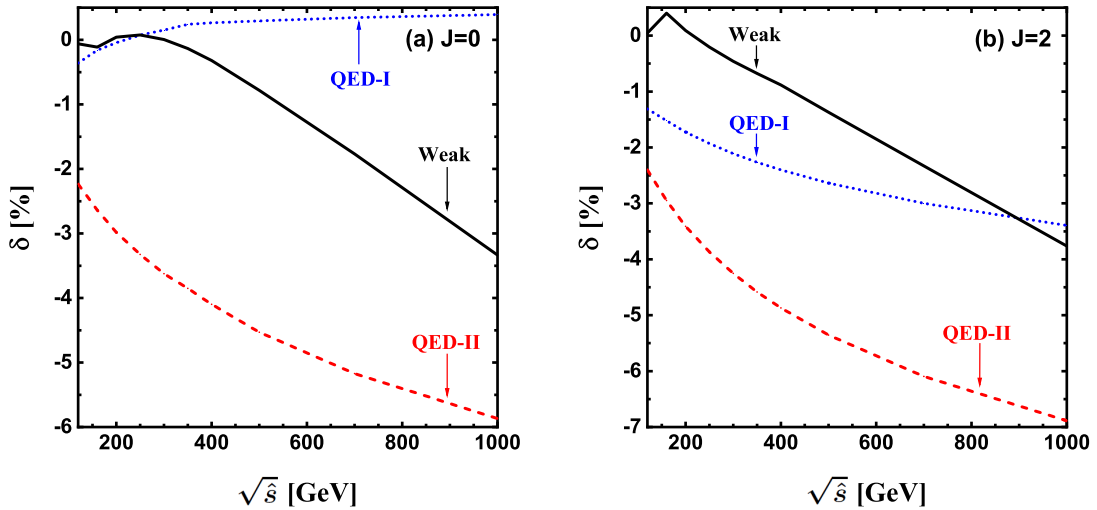


FIG. 4. QED and weak relative corrections in both inclusive and exclusive event selection schemes as functions of the $\gamma\gamma$ colliding energy for $e^+e^-\gamma$ production in (a) $J = 0$ and (b) $J = 2$ $\gamma\gamma$ collisions.

D. Kinematic distributions

The LO, NLO EW corrected energy distributions of the final-state positron in scheme-II and the corresponding EW relative corrections in both scheme-I and -II for the $e^+e^-\gamma$ production in $J = 0$ and $J = 2$ collisions at $\sqrt{\hat{s}} = 500$ GeV PLC are presented in Figs.5 (a) and (b), respectively. As $\sqrt{\hat{s}}$ increases, the LO and NLO EW corrected E_{e^+} distributions for

$J = 0$ $\gamma\gamma$ collision mode decrease gradually, reach their minima at $\sqrt{\hat{s}} \sim 160$ GeV, and then increase rapidly to their maxima at $E_{e^+} \sim \sqrt{\hat{s}}/2 - E_{\gamma,\min} = 240$ GeV, which corresponds to the minimum-energy photon emitted from positron, while the E_{e^+} distributions for $J = 2$ collision mode increases monotonically before reaching their maxima at $\sqrt{\hat{s}} \sim 240$ GeV. The LO, NLO EW corrected scattering angle distributions of the final-state positron and the corresponding EW relative corrections are depicted in Figs.5 (c) and (d). For the $J = 0$ collision mode, both $d\sigma_{\text{LO}}/d\cos\theta_{e^+}$ and $d\sigma_{\text{NLO}}^{(\text{I}, \text{II})}/d\cos\theta_{e^+}$ are symmetric with respect to $\cos\theta_{e^+} = 0$ ³. The corresponding EW relative correction increases from -1.3% to -0.3% as $\cos\theta_{e^+}$ varies from 0 to $\cos 10^\circ = 0.985$ in the inclusive event selection scheme, while it is steady at around -5.5% for $|\cos\theta_{e^+}| < 0.9$ in the exclusive event selection scheme. For the $J = 2$ collision mode, although the LO $\cos\theta_{e^+}$ distribution is also symmetric with respect to $\cos\theta_{e^+} = 0$, the NLO EW correction breaks this forward-backward symmetry. In the exclusive event selection scheme, the EW relative correction is negative and notable ($|\delta_{\text{EW}}^{(\text{II})}| > 5\%$), and can reach about -10% at $\cos\theta_{e^+} \sim 0.5$. The lineshape of the EW relative correction in the inclusive event selection scheme is the same as the exclusive event selection scheme. The QED relative correction contributed by $e^+e^-\gamma\gamma$ events is steady at around 2.8% .

The LO, NLO EW corrected energy and scattering angle distributions of the final-state electron as well as the corresponding EW relative corrections for the $e^+e^-\gamma$ production in $J = 0$ and $J = 2$ collisions at $\sqrt{\hat{s}} = 500$ GeV PLC are plotted in Figs.6 (a)-(d). As expected, all the kinematic distributions of the final-state electron are the same as the corresponding ones of the final-state positron for both $\gamma_+\gamma_+ \rightarrow e^+e^-\gamma$ ($J = 0$) and $\gamma_+\gamma_- \rightarrow e^+e^-\gamma$ ($J = 2$) channels at the LO due to the charge symmetry. However, it should be noted that the charge conjugation is only a Born-level symmetry operation for the $e^+e^-\gamma$ production at the PLC since $\gamma\gamma \rightarrow e^+e^-\gamma$ is a pure QED process at the lowest order, and the charge symmetry will be broken at the EW NLO by weak correction. Consequently, the EW relative corrections to the kinematic distributions of electron differ from the corresponding ones of the positron for the $e^+e^-\gamma$ production in the $J = 0$ $\gamma\gamma$ collision, as shown in the lower panels of Figs.5 (a, c) and Figs.6 (a, c). As stated in Sec.II A, the kinematic behaviors of the final-state electron should be the same as positron for $J = 2$ $\gamma\gamma$ collision mode due to the $\mathcal{CP}+Bose$ symmetry.

³ The forward-backward symmetry of $d\sigma_{\text{NLO}}^{(\text{I})}/d\cos\theta_{e^+}$ can be read off from the lower panel of Fig.5 (c).

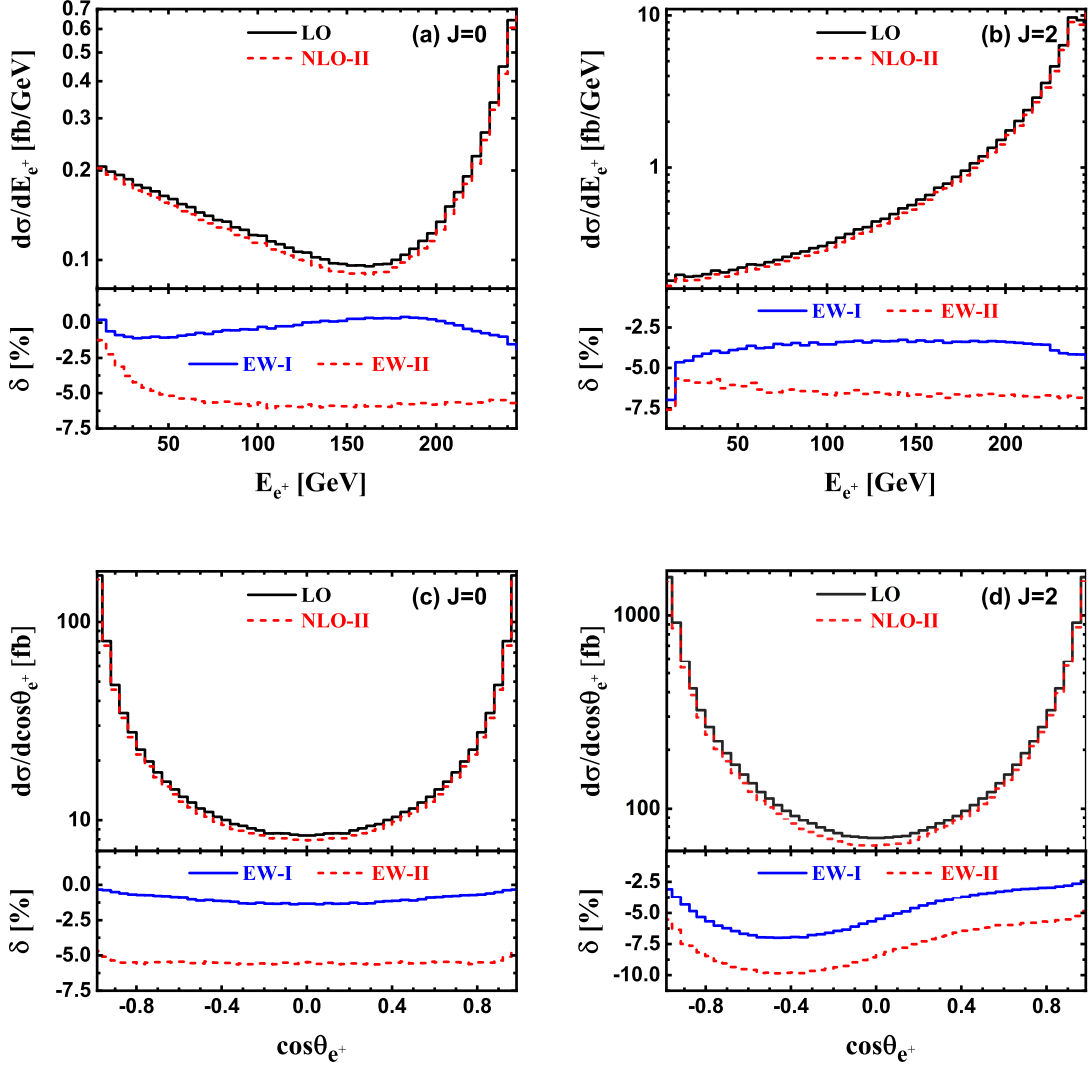


FIG. 5. LO, NLO EW corrected differential distributions of the final-state positron and the corresponding EW relative corrections for the $e^+e^- \gamma$ production at $\sqrt{\hat{s}} = 500$ GeV PLC. (a), (b), (c) and (d) are for the energy and scattering angle distributions in $J = 0$ and $J = 2$ collision modes, respectively.

It can be concluded from Eq.(5) that

$$\frac{d\sigma}{dE_{e^-}} = \frac{d\sigma}{dE_{e^+}} \Big|_{E_{e^+} \rightarrow E_{e^-}} \quad \text{and} \quad \frac{d\sigma}{d\cos\theta_{e^-}} = \frac{d\sigma}{d\cos\theta_{e^+}} \Big|_{\theta_{e^+} \rightarrow \pi - \theta_{e^-}} \quad (16)$$

at both LO and EW NLO. By comparing Figs.6 (b, d) with Figs.5 (b, d) we can see that the numerical results for E_{e^\pm} and $\cos\theta_{e^\pm}$ distributions of the $\gamma_+\gamma_- \rightarrow e^+e^- \gamma$ production channel satisfy Eq.(16) exactly. The consistency of our numerical results with the $\mathcal{CP} + Bose$

symmetry for $e^+e^- \gamma$ production in $J = 2$ $\gamma\gamma$ collision also verifies the correctness of our calculations.

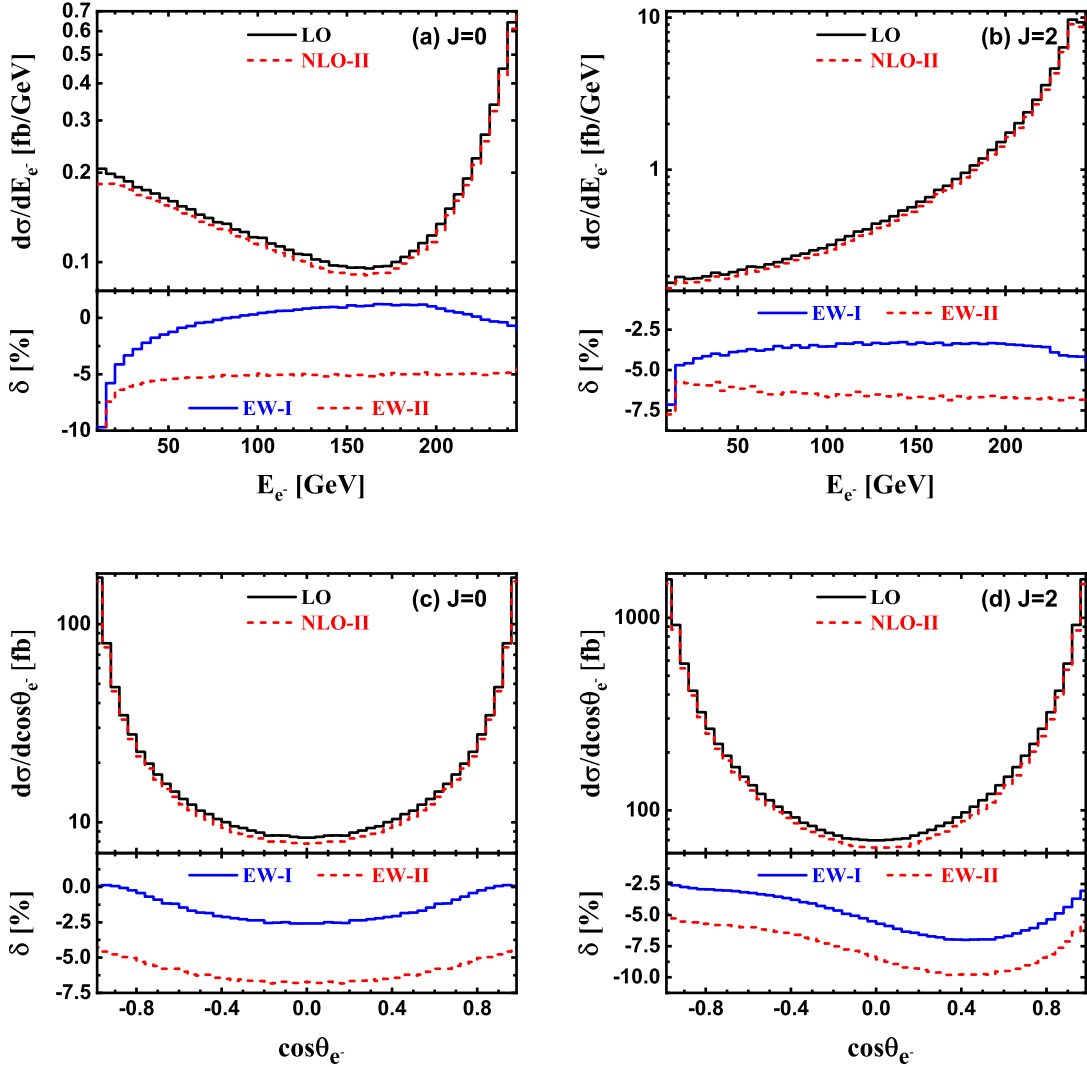


FIG. 6. Same as Fig.5, but for the final-state electron.

For an $e^+e^- \gamma$ event collected in the inclusive event selection scheme, the two photons are called leading and sub-leading photons, respectively, according to their energies in decreasing order (The photon of an $e^+e^- \gamma$ event can also be named as leading photon.). In the upper panels of Figs.7 (a)-(d), we depict the energy and scattering angle distributions of the leading photon for $e^+e^- \gamma$ production in $J = 0$ and $J = 2$ $\gamma\gamma$ collisions at $\sqrt{s} = 500$ GeV PLC at both LO and EW NLO. The corresponding EW relative corrections are provided in the

lower panels. As shown in Figs.7 (a) and (b), the LO and NLO EW corrected energy distributions of the leading photon in scheme-II increase consistently as $\sqrt{\hat{s}}$ increases from 10 to 240 GeV for the $J = 0$ polarization configuration of the incoming photon beams, while decrease gradually as the increase of $\sqrt{\hat{s}}$ in most plotted E_γ region for $J = 2$ $\gamma\gamma$ collision mode. The peak structure at $\sqrt{\hat{s}} \sim 240$ GeV in the EW relative corrections in both inclusive and exclusive event selection schemes can be attributed to the Z resonance effect induced by the loop diagram in Fig.2 (2). At the Z resonance, $M_{e^+e^-} = m_Z$, and thus $E_\gamma = (\hat{s} - m_Z^2)/(2\sqrt{\hat{s}}) \sim 240$ GeV which corresponds to a photon recoiling against an on-shell Z boson. From Figs.7 (c) and (d) we can see that both the LO $\cos\theta_\gamma$ distribution and the NLO EW correction are symmetric with respect to $\cos\theta_\gamma = 0$, and the differential distribution increases rapidly as the increase of $|\cos\theta_\gamma|$. It implies that the leading photon prefers to be produced along the incoming photon beam directions. In the exclusive event selection scheme, the EW relative correction is negative and sizable. It can exceed -6% for $J = 0$ and -7% for $J = 2$, respectively, when the final-state leading photon is produced centrally ($|\cos\theta_\gamma| < 0.5$).

The LO, NLO EW corrected invariant mass and opening angle distributions of the final-state γe^+ system (or more strictly speaking, the final-state leading photon and positron) and the corresponding EW relative corrections for $e^+e^-\gamma$ production via $\gamma_+\gamma_+$ and $\gamma_+\gamma_-$ collisions at $\sqrt{\hat{s}} = 500$ GeV PLC are presented in Figs.8 (a)-(b) separately. For $J = 0$ (i.e., $\gamma_+\gamma_+$) collision mode, the invariant mass distribution of the γe^+ system increases sharply in the low $M_{\gamma e^+}$ region, reaches its maximum at $\sqrt{\hat{s}} \sim 70$ GeV, and then decreases gradually as $M_{\gamma e^+}$ increases to around 260 GeV. Subsequently, the invariant mass distribution increases rapidly as the increase of $M_{\gamma e^+}$. The EW relative correction in the exclusive event selection scheme is steady at around -5% in most of the $M_{\gamma e^+}$ region. For $J = 2$ (i.e., $\gamma_+\gamma_-$) collision mode, there are two sharp peaks located at $M_{\gamma e^+} \sim 20$ GeV and $M_{\gamma e^+} \sim 100$ GeV in the γe^+ invariant mass distribution. As we know, the invariant mass of the final-state γe^+ system is given by

$$M_{\gamma e^+} \approx M_{\gamma e^+}^{(\text{LO})} = \sqrt{\hat{s} + m_e^2 - 2E_{e^-}\sqrt{\hat{s}}}, \quad (17)$$

where $M_{\gamma e^+}^{(\text{LO})}$ is the lowest-order approximation of $M_{\gamma e^+}$. From Eq.(17) we can see that $M_{\gamma e^+} \sim 20$ GeV and $M_{\gamma e^+} \sim 100$ GeV are equivalent to $E_{e^-} \sim 250$ GeV and $E_{e^-} \sim 240$ GeV, respectively. It is evident that those two peaks in the γe^+ invariant mass distribution can be attributed to the highest-energy electron ($E_{e^-} \sim \sqrt{\hat{s}}/2$) and a minimum-energy photon

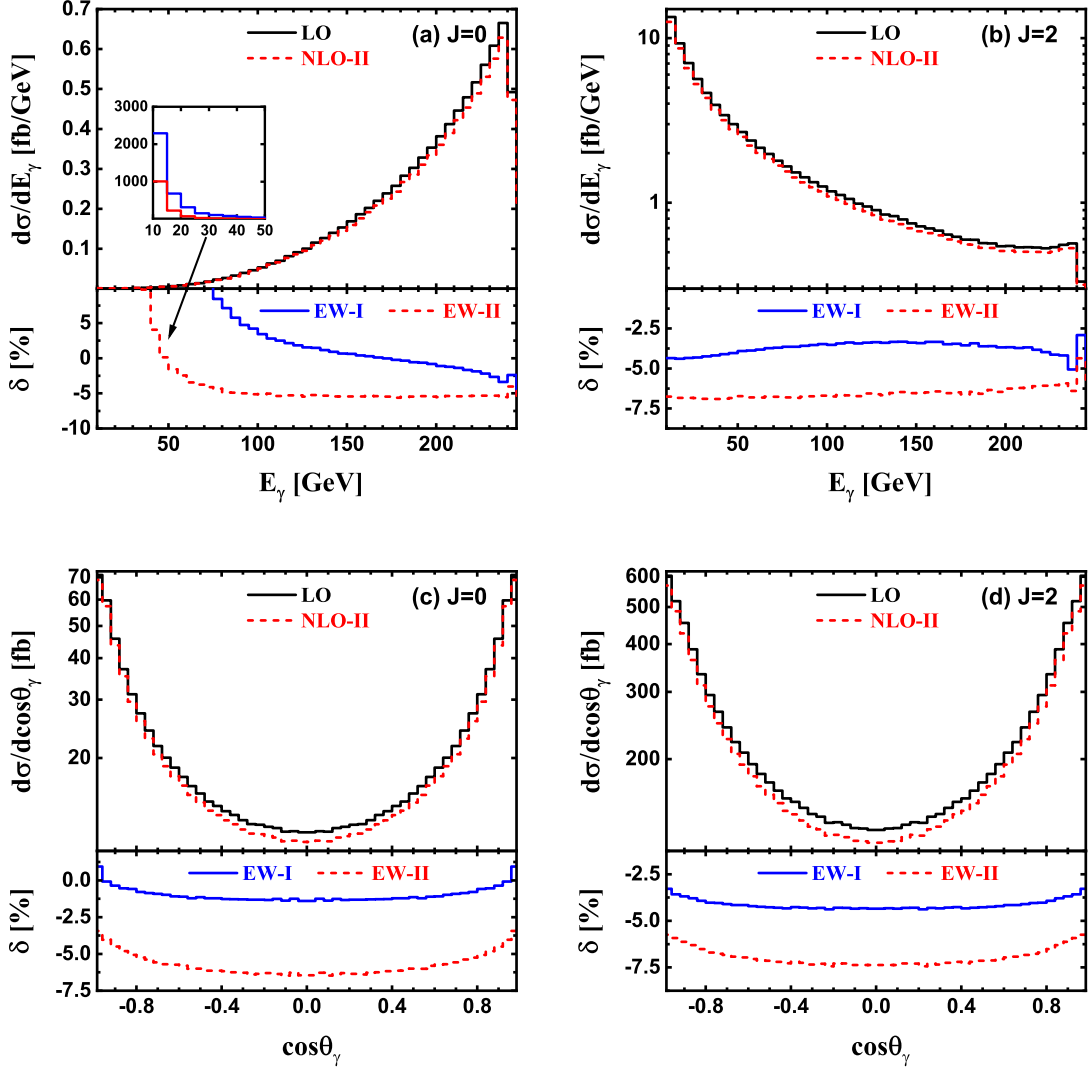


FIG. 7. Same as Fig.5, but for the final-state leading photon.

emitted from electron ($E_{e^-} \sim \sqrt{\hat{s}}/2 - E_{\gamma, \min}$), respectively. Moreover, we can see from the upper plots of Figs.8 (c) and (d) that the angular distributions of the final-state positron and leading photon are highly correlated. The positron and leading photon prefer to be produced back-to-back in the $J = 0$ $\gamma\gamma$ collision, while tend to be produced in the same direction or back-to-back in the $J = 2$ $\gamma\gamma$ collision. It is worth mentioning that the EW relative correction in the exclusive event selection scheme is relatively stable in the entire $\theta_{\gamma e^+}$ region, especially for the $J = 2$ collision mode.

The differential cross sections with respect to the invariant mass and opening angle of

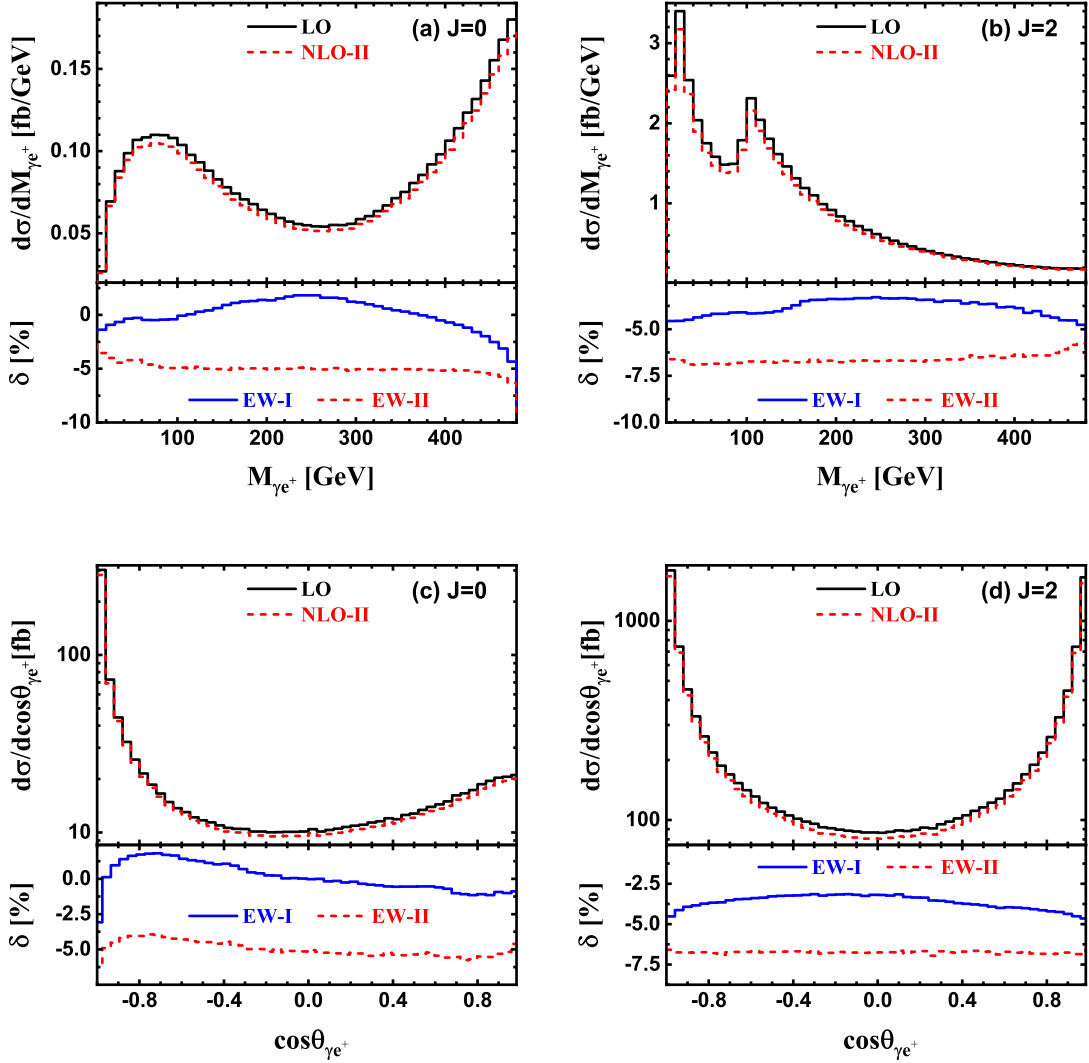


FIG. 8. LO, NLO EW corrected invariant mass and opening angle distributions of the final-state γe^+ system and the corresponding EW relative corrections for the $e^+e^-\gamma$ production in $J = 0$ and $J = 2$ $\gamma\gamma$ collisions at $\sqrt{\hat{s}} = 500$ GeV PLC.

the final-state γe^- system as well as the corresponding EW relative corrections are also provided in Figs.9 (a)-(d) for comparison. As expected, the invariant mass and opening angle distributions of the final-state γe^- system are exactly the same as the corresponding ones of γe^+ system at the LO due to the charge conservation in the electromagnetic interaction. For the $\gamma_+\gamma_+ \rightarrow e^+e^-\gamma$ (i.e., $J = 0$) production channel, the EW relative corrections to $M_{\gamma e^-}$ and $\cos\theta_{\gamma e^-}$ distributions are significantly differ from the EW relative corrections to

$M_{\gamma e^+}$ and $\cos\theta_{\gamma e^+}$ distributions, as shown in the lower panels of Figs.8 (a, c) and Figs.9 (a, c), due to the charge symmetry violation in weak interaction. In contrast, the EW relative corrections to the kinematic distributions of γe^- and γe^+ systems are exactly the same for $\gamma_+\gamma_- \rightarrow e^+e^-\gamma$ (i.e., $J = 2$) production channel, as shown in the lower panels of Figs.8 (b, d) and Figs.9 (b, d), because of the $\mathcal{CP}+Bose$ symmetry. The numerical consistency between the kinematic distributions of the final-state γe^- and γe^+ systems in the $\gamma_+\gamma_-$ collision reconfirms the conclusion declared in Sec.II A.

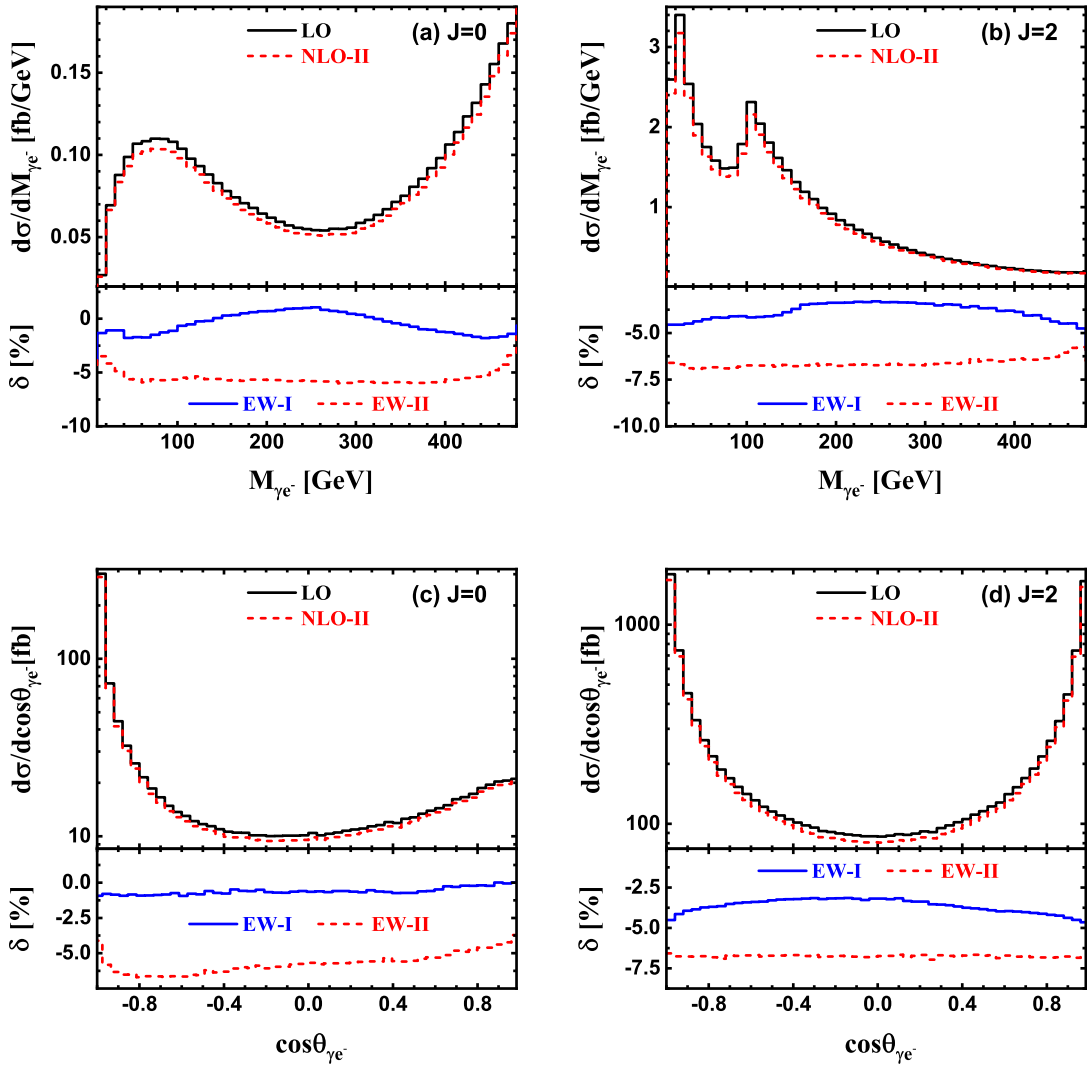


FIG. 9. Same as Fig.8, but for the final-state γe^- system.

E. Parent process $ee \rightarrow \gamma\gamma \rightarrow e^+e^-\gamma$

Now we turn to the discussion of the parent process $ee \rightarrow \gamma\gamma \rightarrow e^+e^-\gamma$. The differential cross section for $ee \rightarrow \gamma\gamma \rightarrow e^+e^-\gamma$ with respect to a kinematic variable ζ can be expressed as

$$\frac{d\sigma}{d\zeta} = \frac{d\sigma^{(0)}}{d\zeta} + \frac{d\sigma^{(2)}}{d\zeta}, \quad (18)$$

where $d\sigma^{(0)}/d\zeta$ and $d\sigma^{(2)}/d\zeta$ represent the contributions from $J = 0$ and $J = 2$ $\gamma\gamma$ collision modes, respectively. Considering that the two back-scattered photon beams are partially polarized, $d\sigma^{(0)}/d\zeta$ and $d\sigma^{(2)}/d\zeta$ are calculated by

$$\begin{aligned} \frac{d\sigma^{(J)}}{d\zeta}(s) = & \sum_{\lambda_1=(-1)^{\frac{1}{2}}\lambda_2} \int_{2m_e/\sqrt{s}}^{x_{\max}} \frac{zdz}{2} \int_{z^2/x_{\max}}^{x_{\max}} \frac{dx}{x} \phi_{\gamma/e}(x) \phi_{\gamma/e}(z^2/x) \\ & \left[1 + \lambda_1 \mathcal{P}_\gamma(x)\right] \left[1 + \lambda_2 \mathcal{P}_\gamma(z^2/x)\right] \frac{d\hat{\sigma}^{\lambda_1\lambda_2}}{d\zeta}(\hat{s} = z^2s), \quad (J = 0, 2) \end{aligned} \quad (19)$$

When discussing the angular distributions of final particles in the c.m. frame of the initial ee system, the reference direction can be chosen as either of the two electron beam directions due to the forward-backward symmetry.

In Figs.10 (a) and (b), we depict the LO, NLO EW corrected integrated cross sections from the $J = 0$ and $J = 2$ $\gamma\gamma$ collisions in the exclusive event selection scheme as well as the corresponding EW relative corrections in both inclusive and exclusive event selection schemes as functions of the ee c.m. colliding energy for $ee \rightarrow \gamma\gamma \rightarrow e^+e^-\gamma$. The integrated contributions from $J = 0$ and $J = 2$ $\gamma\gamma$ collisions increase at first, reach their maxima at $\sqrt{s} \sim 140$ and 200 GeV, respectively, and then decrease rapidly as \sqrt{s} increases. In the exclusive event selection scheme, the EW relative correction to the integrated cross section from the $J = 0$ $\gamma\gamma$ collision is relatively stable as $\sqrt{s} \in [400, 1000]$ GeV, varying in the range of $[-3.2\%, -2.7\%]$. Compared to $J = 0$, the EW relative correction to the integrated cross section from $J = 2$ $\gamma\gamma$ collision is more sensitive to the ee c.m. colliding energy. It decreases approximately linearly from about -2.5% to about -3.8% as \sqrt{s} increases from 400 GeV to 1 TeV. Similar to the discussion on $\gamma\gamma \rightarrow e^+e^-\gamma$, we also separately provide weak and QED relative corrections to the parent process $ee \rightarrow \gamma\gamma \rightarrow e^+e^-\gamma$ for both $J = 0$ and $J = 2$ polarization configurations of the Compton back-scattered photons. As shown in Figs.11 (a) and (b), the weak relative correction is small ($|\delta_W| < 0.5\%$) and the full NLO EW correction is dominated by the negative QED correction for both polarization modes of

the back-scattered photons in the entire plotted \sqrt{s} region ($120 \text{ GeV} < \sqrt{s} < 1000 \text{ GeV}$). In the exclusive event selection scheme, the QED relative correction reaches its maximum of about -1.9% at $\sqrt{s} \sim 150 \text{ GeV}$ and is roughly steady at -2.9% as $\sqrt{s} \in [500, 1000] \text{ GeV}$ for $J = 0$ polarization of the back-scattered photons, while it decreases gradually from its maximum of about -1.9% to approximately -3.4% as \sqrt{s} increases from 180 GeV to 1 TeV for the $J = 2$ $\gamma\gamma$ polarization mode. As is well known, the maximum energy fraction of the back-scattered photon is given by [5]

$$x_{\max} = \frac{4E_e E_0}{4E_e E_0 + m_e^2}, \quad (20)$$

where E_e represents the electron beam energy and E_0 denotes the energy of the laser photon. In this study, we take $E_0 = 1.17 \text{ eV}$ (i.e., the laser wave length $\lambda = 1.06 \mu\text{m}$). At $\sqrt{s} = 120 \text{ GeV}$, the maximum c.m. colliding energy of the back-scattered photon beams is only approximately 60 GeV , thus the NLO QED contribution of the $e^+e^-\gamma\gamma$ events is too tiny to be ignored due to the small phase space of the $e^+e^-\gamma\gamma$ four-body final state. As \sqrt{s} increases, the QED relative correction contributed by $e^+e^-\gamma\gamma$ events (i.e., $\delta_{\text{QED}}^{(I)} - \delta_{\text{QED}}^{(II)}$) becomes more and more notable and compensates the negative EW correction from $e^+e^-\gamma$ events. As $\sqrt{s} \in [600, 1000] \text{ GeV}$, the QED relative correction in the inclusive event selection scheme is steady at around -1.1% and -1.8% for $J = 0$ and $J = 2$, respectively. Finally, in Table II and Table III, we present in detail the production cross sections and the corresponding NLO relative corrections for $ee \rightarrow \gamma\gamma \rightarrow e^+e^-\gamma$ at $\sqrt{s} = 250, 500$ and 1000 GeV , which correspond to the three stages of the ILC [2]. For more details on the kinematic distributions of final products of $ee \rightarrow \gamma\gamma \rightarrow e^+e^-\gamma$, refer to the Appendix section of this article.

\sqrt{s} [GeV]	σ_{LO} [fb]	$\sigma_{\text{NLO}}^{(I)}$ [fb]	$\sigma_{\text{NLO}}^{(II)}$ [fb]	$\delta_{\text{EW}}^{(I)}$ [%]	$\delta_{\text{EW}}^{(II)}$ [%]	$\delta_{\text{QED}}^{(I)}$ [%]	$\delta_{\text{QED}}^{(II)}$ [%]	δ_{W} [%]
250	131.93	130.46	128.80	-1.11	-2.37	-1.05	-2.31	-0.06
500	44.729	44.260	43.452	-1.05	-2.85	-1.01	-2.81	-0.04
1000	11.195	11.041	10.838	-1.38	-3.19	-1.14	-2.95	-0.24

TABLE II. LO, NLO EW corrected cross sections and the corresponding NLO relative corrections for $ee \rightarrow \gamma\gamma \rightarrow e^+e^-\gamma$ via $J = 0$ collision of Compton back-scattered photons at $\sqrt{s} = 250, 500$ and 1000 GeV .

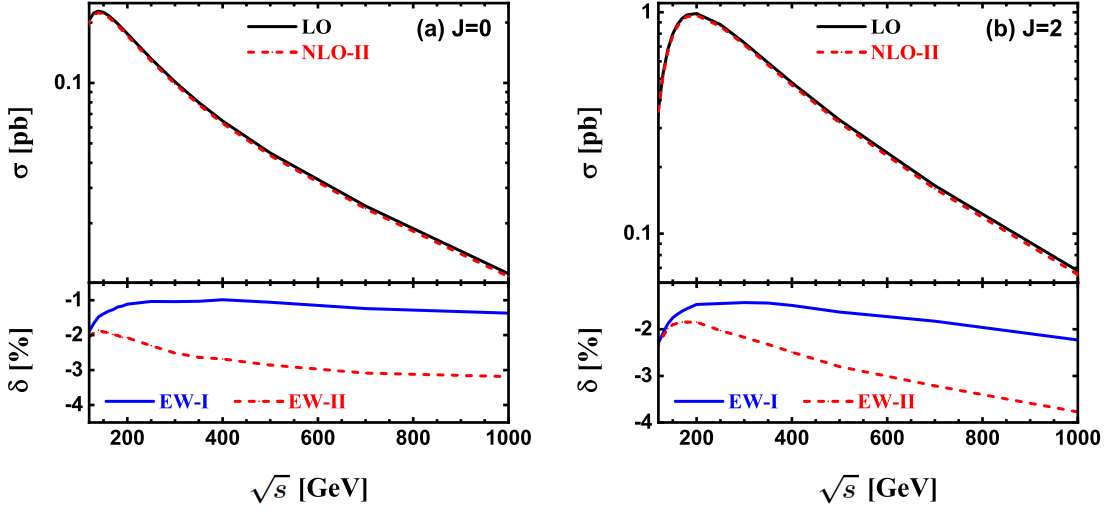


FIG. 10. LO, NLO EW corrected integrated cross sections from (a) $J = 0$ and (b) $J = 2$ $\gamma\gamma$ collisions in scheme-II and the corresponding EW relative corrections in both scheme-I and -II as functions of \sqrt{s} for $ee \rightarrow \gamma\gamma \rightarrow e^+e^-\gamma$.

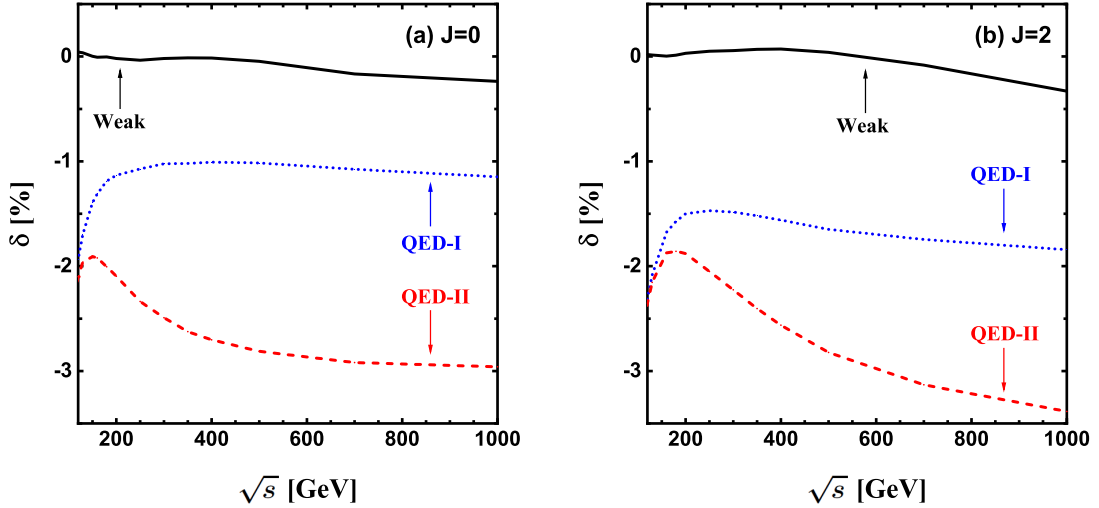


FIG. 11. QED and weak relative corrections to the integrated cross sections from (a) $J = 0$ and (b) $J = 2$ $\gamma\gamma$ collisions in both scheme-I and -II as functions of \sqrt{s} for $ee \rightarrow \gamma\gamma \rightarrow e^+e^-\gamma$.

\sqrt{s} [GeV]	σ_{LO} [fb]	$\sigma_{\text{NLO}}^{(\text{I})}$ [fb]	$\sigma_{\text{NLO}}^{(\text{II})}$ [fb]	$\delta_{\text{EW}}^{(\text{I})}$ [%]	$\delta_{\text{EW}}^{(\text{II})}$ [%]	$\delta_{\text{QED}}^{(\text{I})}$ [%]	$\delta_{\text{QED}}^{(\text{II})}$ [%]	δ_{W} [%]
250	880.36	867.61	862.51	-1.45	-2.03	-1.48	-2.06	+0.03
500	326.15	320.84	317.01	-1.63	-2.80	-1.63	-2.80	+0.00
1000	67.879	66.366	65.319	-2.23	-3.77	-1.86	-3.40	-0.37

TABLE III. Same as Table II, but for $J = 2$ collision mode of back-scattered photons.

IV. SUMMARY

$\gamma\gamma \rightarrow l^+l^-\gamma$ as well as $\gamma\gamma \rightarrow l^+l^-$ is an ideal channel for calibrating the beam luminosity of the Photon Linear Collider, especially for the $J = 0$ polarization of the incident photon beams. In this paper, we present the full $\mathcal{O}(\alpha)$ EW corrected integrated cross sections and some kinematic distributions of final products for the $e^+e^-\gamma$ production in $\gamma\gamma$ collision. The production rate of $e^+e^-\gamma$ in $J = 2$ $\gamma\gamma$ collision is significantly larger than that in $J = 0$ collision mode. In the exclusive event selection scheme, the NLO EW correction is dominated by the QED contribution; the entire EW relative correction is sensitive to the $\gamma\gamma$ c.m. colliding energy and can exceed -10% at a TeV PLC for both $J = 0$ and $J = 2$ polarization configurations of photon beams. The kinematic behaviors of the final products in $J = 0$ $\gamma\gamma$ collision are quite different from those in $J = 2$ collision. At $\sqrt{\hat{s}} = 500$ GeV, the EW relative correction is about $-7\% \sim -5\%$ in most of the final-state phase space and can even reach around -10% in some specific phase-space regions. We can conclude that the NLO EW correction exerts important impact on both integrated and differential cross sections, and thus is significant in the precise determination of incoming photon beam luminosity at PLC.

Acknowledgments:

This work is supported in part by the National Natural Science Foundation of China (Grants No. 11775211 and No. 12061141005) and the CAS Center for Excellence in Particle Physics (CCEPP).

[1] V. I. Telnov, Nucl. Instrum. Meth. A **355**, 3 (1995).

- [2] D. M. Asner *et al.*, ILC Higgs White Paper, *Community Summer Study 2013: Snowmass on the Mississippi*, (2013), arXiv:1310.0763 [hep-ph].
- [3] I. F. Ginzburg, G. L. Kotkin, V. G. Serbo, and V. I. Telnov, Nucl. Instrum. Meth. **205**, 47 (1983).
- [4] I. F. Ginzburg, G. L. Kotkin, S. L. Panfil, V. G. Serbo, and V. I. Telnov, Nucl. Instrum. Meth. A **219**, 5 (1984).
- [5] A. F. Żarnecki, Acta Phys. Polon. B **34**, 2741 (2003), arXiv:hep-ex/0207021 [hep-ex].
- [6] E. Boos, Nucl. Instrum. Meth. A **472**, 22 (2001), arXiv:hep-ph/0009100 [hep-ph].
- [7] M. M. Velasco *et al.*, eConf **C010630**, E3005 (2001), arXiv:hep-ex/0111055 [hep-ex].
- [8] P. Niezurawski, eConf **C050318**, 0503 (2005), arXiv:hep-ph/0507004 [hep-ph].
- [9] B. Badelek *et al.* (ECFA/DESY Photon Collider Working Group), Int. J. Mod. Phys. A **19**, 5097 (2004), arXiv:hep-ex/0108012 [hep-ex].
- [10] V. I. Telnov, Acta Phys. Polon. B **37**, 1049 (2006), arXiv:physics/0604108 [physics].
- [11] Y. Yasui, I. Watanabe, J. Kodaira, and I. Endo, Nucl. Instrum. Meth. A **335**, 385 (1993), arXiv:hep-ph/9212312 [hep-ph].
- [12] A. Denner and S. Dittmaier, Eur. Phys. J. C **9**, 425 (1999), arXiv:hep-ph/9812411 [hep-ph].
- [13] M. Demirci and M. F. Mustamin, Phys. Rev. D **103**, 113004 (2021), arXiv:2105.05340 [hep-ph].
- [14] S. Dittmaier, Phys. Rev. D **59**, 016007 (1998), arXiv:hep-ph/9805445 [hep-ph].
- [15] D. M. Asner, J. B. Gronberg, and J. F. Gunion, Phys. Rev. D **67**, 035009 (2003), arXiv:hep-ph/0110320 [hep-ph].
- [16] A. V. Pak, D. V. Pavluchenko, S. S. Petrosyan, V. G. Serbo, and V. I. Telnov, Nucl. Phys. Proc. Suppl. **126**, 379 (2004), arXiv:hep-ex/0301037 [hep-ex].
- [17] V. Makarenko and T. V. Shishkina, arXiv:hep-ph/0310104 [hep-ph].
- [18] V. Makarenko, K. Mönig, and T. Shishkina, Eur. Phys. J. C **32S1**, 143 (2003), arXiv:hep-ph/0306135 [hep-ph].
- [19] P. H. Kiem *et al.*, Phys. Lett. B **740**, 192 (2015), arXiv:1403.6557 [hep-ph].
- [20] D. Bardin, Y. Dydyshka, L. Kalinovskaya, L. Rumyantsev, R. Sadykov, A. Arbuzov, and S. Bondarenko, Phys. Rev. D **98**, 013001 (2018), arXiv:1801.00125 [hep-ph].
- [21] G. Moortgat-Pick *et al.*, Phys. Rept. **460**, 131 (2008), arXiv:hep-ph/0507011 [hep-ph].
- [22] P. De Causmaecker, R. Gastmans, W. Troost, and T. T. Wu, Phys. Lett. B **105**, 215 (1981).

- [23] F. A. Berends, R. Kleiss, P. De Causmaecker, R. Gastmans, W. Troost, and T. T. Wu, Nucl. Phys. B **206**, 61 (1982).
- [24] T. Hahn and M. Pérez-Victoria, Comput. Phys. Commun. **118**, 153 (1999), arXiv:hep-ph/9807565 [hep-ph].
- [25] G. J. van Oldenborgh, Comput. Phys. Commun. **66**, 1 (1991).
- [26] T. Hahn, Comput. Phys. Commun. **140**, 418 (2001), arXiv:hep-ph/0012260 [hep-ph].
- [27] G. 't Hooft and M. Veltman, Nucl. Phys. B **44**, 189 (1972).
- [28] A. Denner and S. Dittmaier, Nucl. Phys. B **658**, 175 (2003), arXiv:hep-ph/0212259 [hep-ph].
- [29] G. Passarino and M. Veltman, Nucl. Phys. B **160**, 151 (1979).
- [30] D. T. Nhung, L. D. Ninh, and M. M. Weber, JHEP **12**, 096, arXiv:1307.7403 [hep-ph].
- [31] A. Denner, Fortschr. Phys. **41**, 307 (1993), arXiv:0709.1075 [hep-ph].
- [32] T. D. Lee and M. Nauenberg, Phys. Rev. **133**, B1549 (1964).
- [33] T. Kinoshita and A. Ukawa, Lect. Notes Phys. **39**, 55 (1975).
- [34] S. Catani and M. H. Seymour, Phys. Lett. B **378**, 287 (1996), arXiv:hep-ph/9602277 [hep-ph].
- [35] S. Catani and M. H. Seymour, Nucl. Phys. B **485**, 291 (1997), [Erratum: Nucl. Phys. B 510, 503 (1998)], arXiv:hep-ph/9605323 [hep-ph].
- [36] S. Dittmaier, Nucl. Phys. B **565**, 69 (2000), arXiv:hep-ph/9904440 [hep-ph].
- [37] S. Dittmaier, A. Kabelschacht, and T. Kasprzik, Nucl. Phys. B **800**, 146 (2008), arXiv:0802.1405 [hep-ph].
- [38] Z. Nagy and Z. Trócsányi, Phys. Rev. D **59**, 014020 (1999), [Erratum: Phys.Rev.D 62, 099902 (2000)], arXiv:hep-ph/9806317 [hep-ph].
- [39] Z. Nagy, Phys. Rev. D **68**, 094002 (2003), arXiv:hep-ph/0307268 [hep-ph].
- [40] B. W. Harris and J. F. Owens, Phys. Rev. D **65**, 094032 (2002), arXiv:hep-ph/0102128 [hep-ph].
- [41] I. F. Ginzburg and G. L. Kotkin, Eur. Phys. J. C **13**, 295 (2000), arXiv:hep-ph/9905462 [hep-ph].
- [42] P. A. Zyla *et al.* (Particle Data Group), Prog. Theor. Exp. Phys. **2020**, 083C01 (2020).
- [43] F. Jegerlehner, arXiv:hep-ph/0105283 [hep-ph].
- [44] J. Alwall, R. Frederix, S. Frixione, V. Hirschi, F. Maltoni, O. Mattelaer, H. S. Shao, T. Stelzer, P. Torrielli, and M. Zaro, JHEP **07**, 079, arXiv:1405.0301 [hep-ph].
- [45] A. Denner and S. Pozzorini, Eur. Phys. J. C **18**, 461 (2001), arXiv:hep-ph/0010201 [hep-ph].

[46] A. Denner and S. Pozzorini, Eur. Phys. J. C **21**, 63 (2001), arXiv:hep-ph/0104127 [hep-ph].

APPENDIX

In Figs.12 - 16 we present the LO, NLO EW corrected kinematic distributions of the final-state positron, electron and leading photon as well as the corresponding EW relative corrections for $ee \rightarrow \gamma\gamma \rightarrow e^+e^-\gamma$ via $J = 0$ and $J = 2$ collisions of Compton back-scattered photons at $\sqrt{s} = 500$ GeV separately. As expected, the kinematic distributions of e^- and γe^- system are the same as the corresponding ones of e^+ and γe^+ system at both LO and EW NLO within the calculation errors for the $J = 2$ polarization configuration of back-scattered photons.

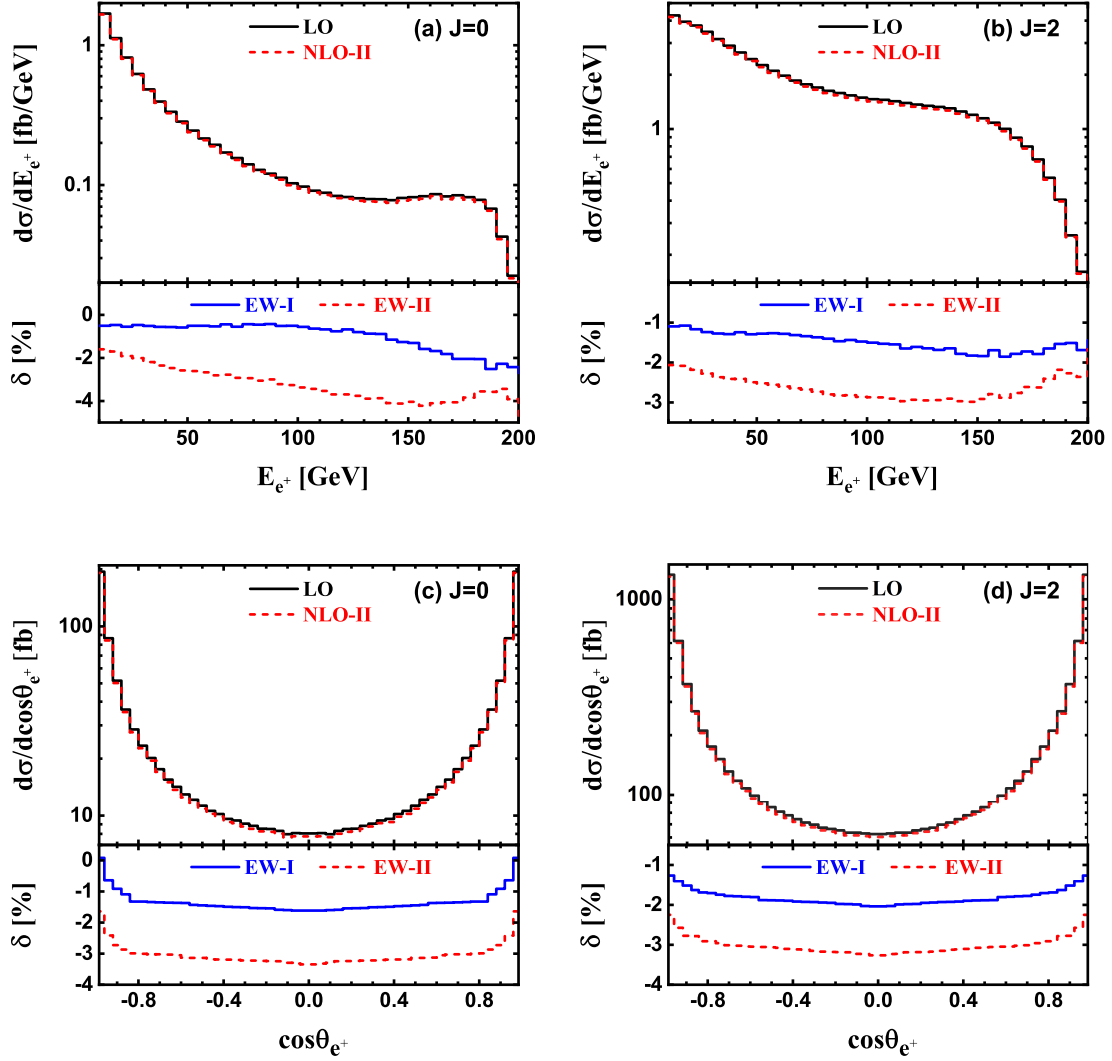


FIG. 12. LO, NLO EW corrected energy and angular distributions of the final-state positron and the corresponding EW relative corrections for $ee \rightarrow \gamma\gamma \rightarrow e^+e^-\gamma$ via $J = 0$ and $J = 2$ collisions of Compton back-scattered photons at $\sqrt{s} = 500$ GeV.

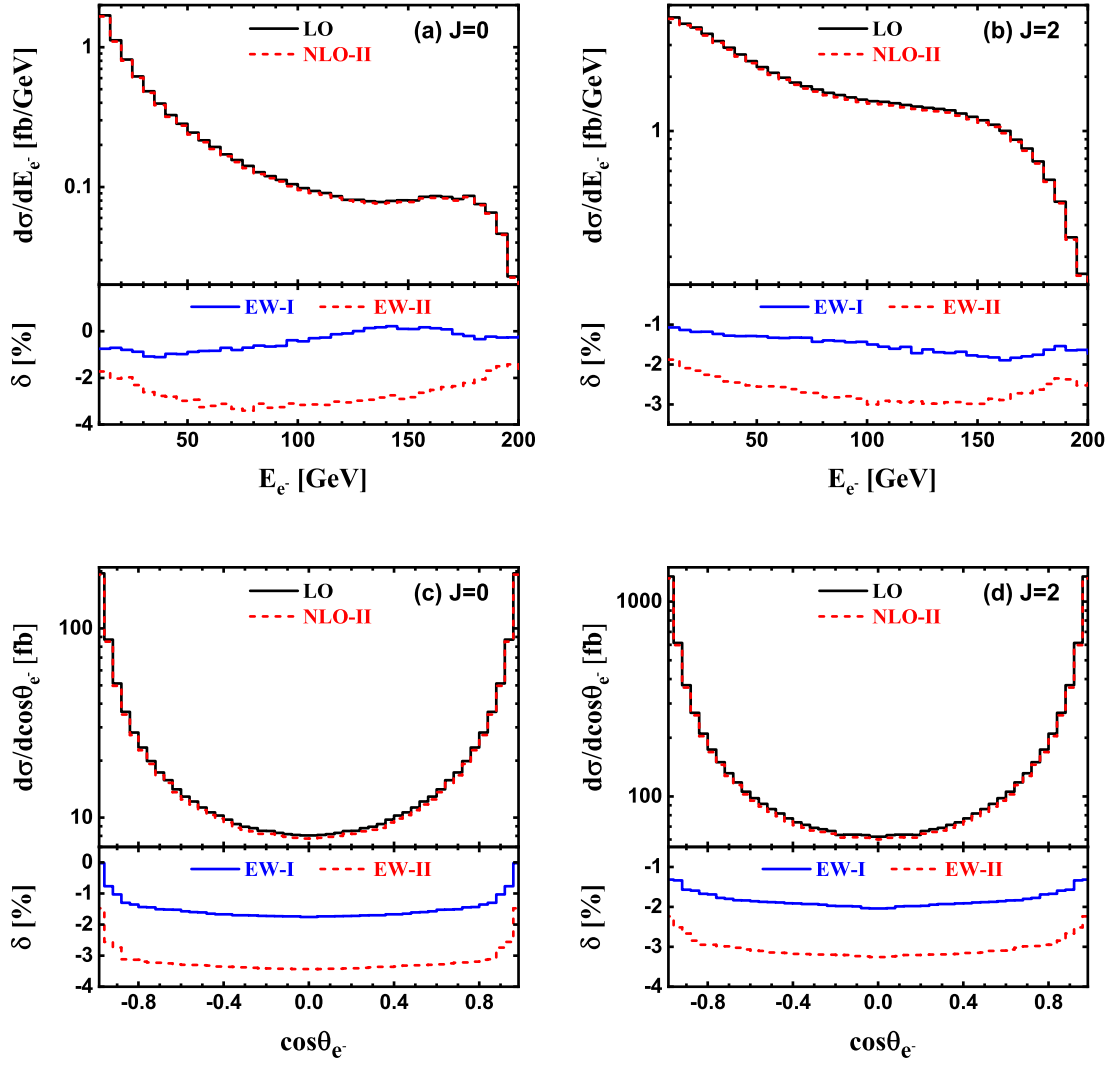


FIG. 13. Same as Fig.12, but for the final-state electron.

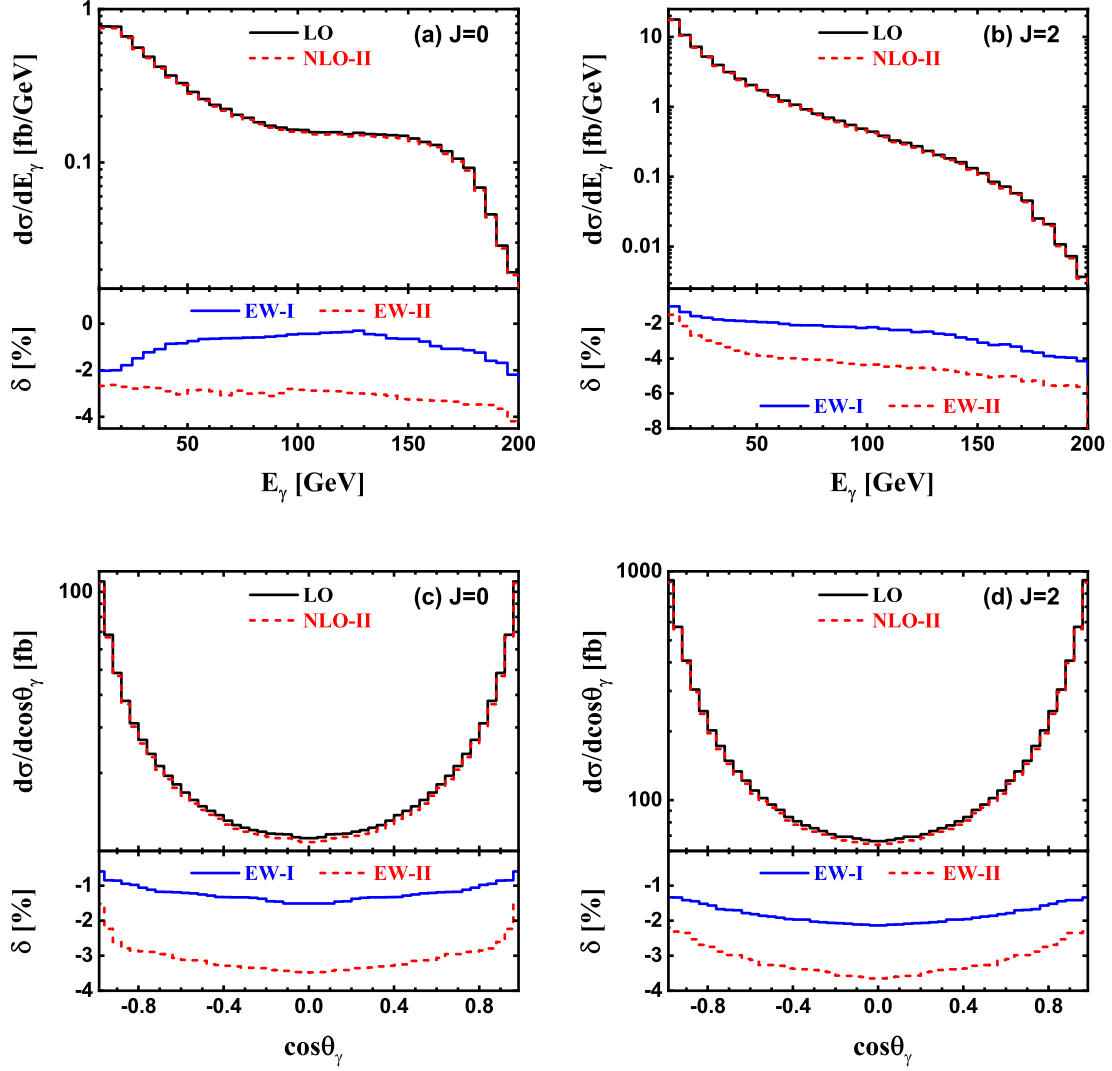


FIG. 14. Same as Fig.12, but for the final-state leading photon.

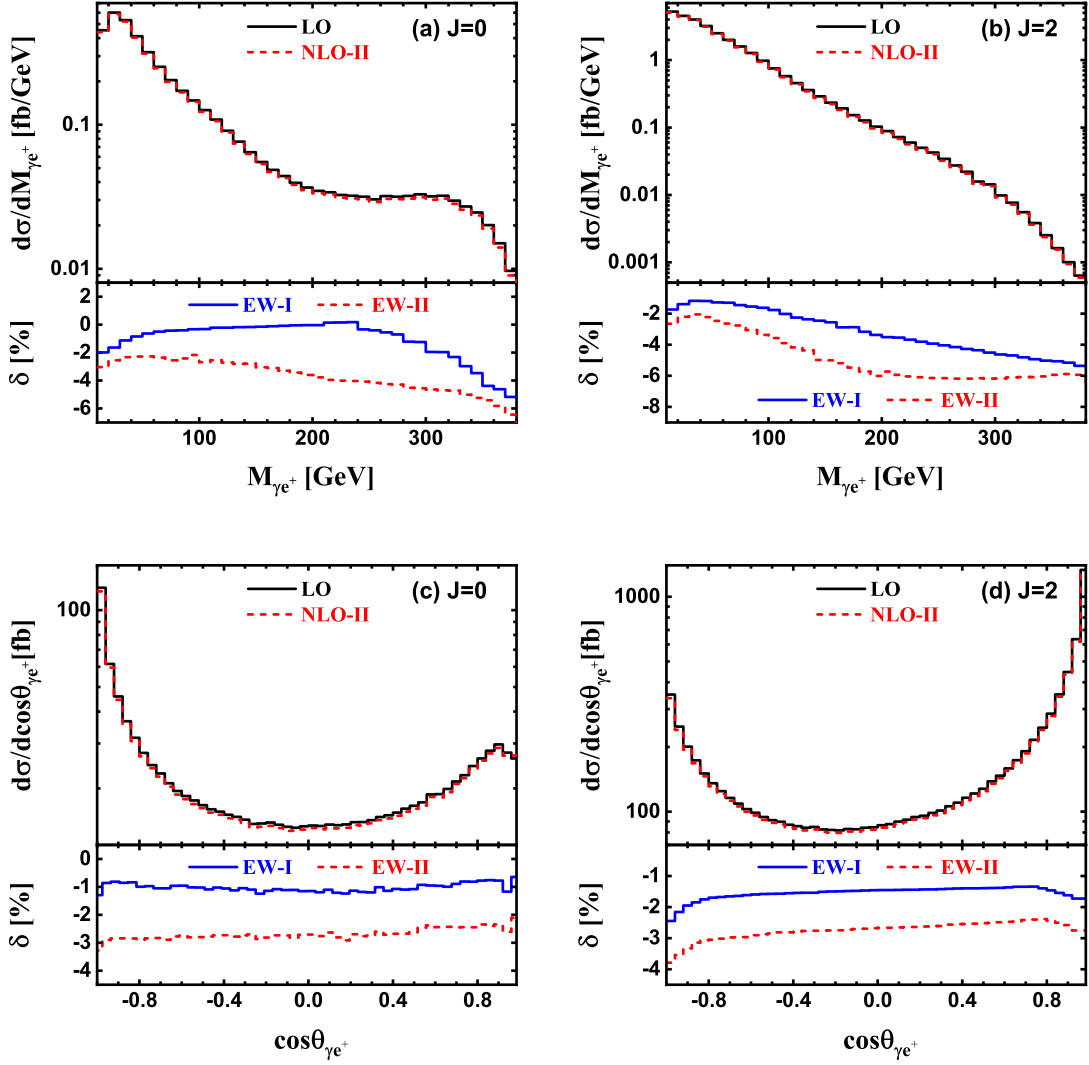


FIG. 15. LO, NLO EW corrected invariant mass and opening angle distributions of the final-state γe^+ system and the corresponding EW relative corrections for $ee \rightarrow \gamma\gamma \rightarrow e^+e^-\gamma$ via $J = 0$ and $J = 2$ collisions of Compton back-scattered photons at $\sqrt{s} = 500$ GeV.

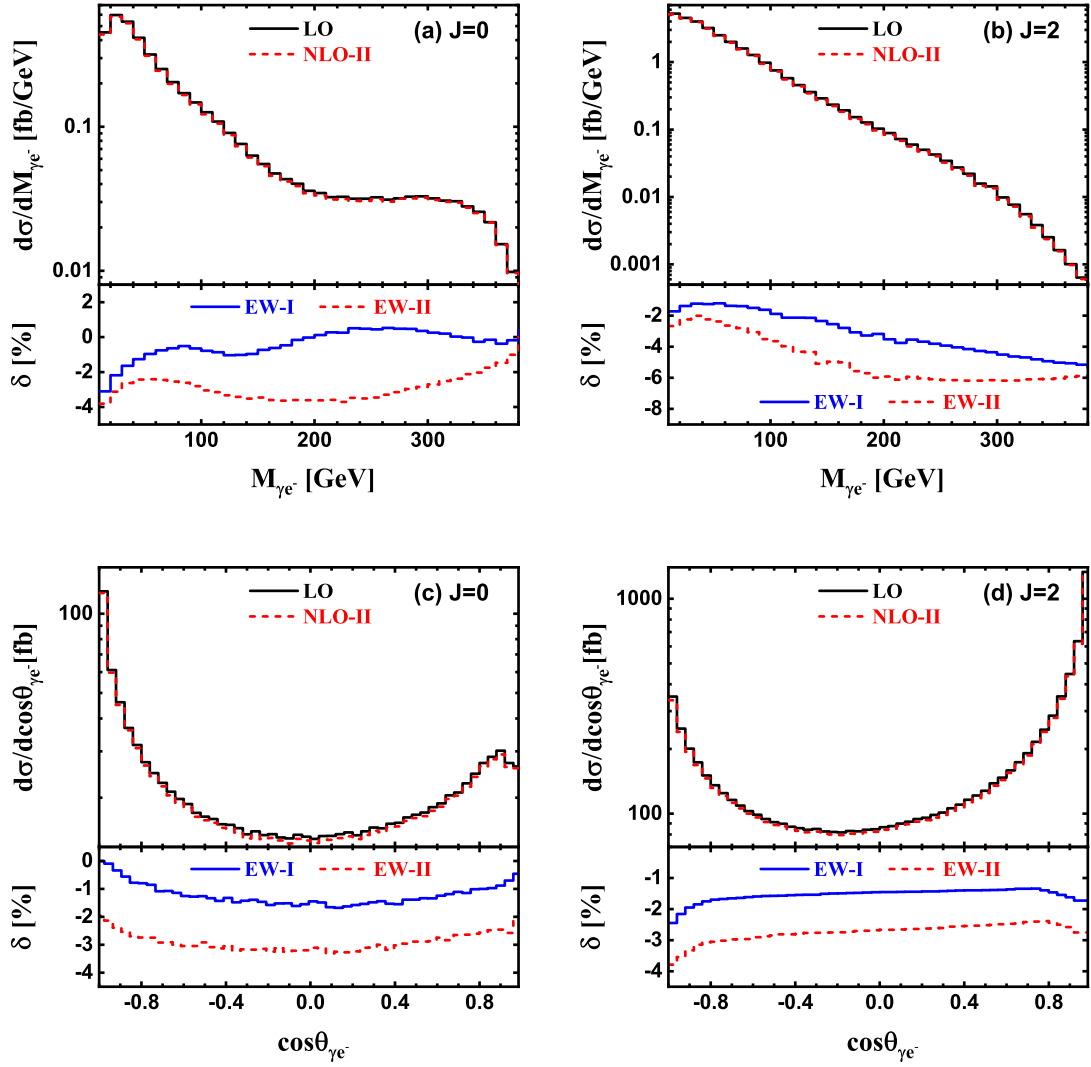


FIG. 16. Same as Fig.15, but for the final-state γe^- system.